AD A055197

FOR FURTHER TRAN

DDC

JUN 19 1978

E

UNITED STATES AIR FORCE
AIR UNIVERSITY
AIR FORCE INSTITUTE OF TECHNOLOGY
Wright-Patterson Air Force Base, Ohio

78 06 13 043

①

⑥ ANALYSIS OF MONOPOLE ANTENNA ARRAYS

ON CYLINDERS BY THE

GEOMETRICAL THEORY OF DIFFRACTION.

⑨ Master's THESIS,

⑭ AFIT/GE/EE/77-41 ⑩ Bruce A. Thieman
2nd Lt   USAF

D D C

RECEIVED
JUN 19 1978

E

⑪ Dec 77   ⑫ 77p.

78 06 13 043

1473

012 225

〈B

ANALYSIS OF MONOPOLE ANTENNA ARRAYS

ON CYLINDERS BY THE

GEOMETRICAL THEORY OF DIFFRACTION

THESIS

Presented to the Faculty of the School of Engineering

of the Air Force Institute of Technology

Air University

in Partial Fulfillment of the

Requirements for the Degree of

Master of Science

by

Bruce A. Thieman, B.S.

2nd Lt   USAF

Graduate Electrical Engineering

December 1977

Preface

This investigation demonstrated the capability of the Geometrical Theory of Diffraction (GTD) to analyze the fields due to monopole arrays on cylinders. Although one of the principle arguments for the use of the GTD method to solve for the field equations was its requirement for less computer usage compared to alternative methods, a computer, as such, was not used.

In this regard I would like to thank Mr. Robert Barham for the use of his HP-67 programable calculator. I would also like to thank Professor Kouyoumjian at Ohio State for his comments and his help in obtaining many of the sources on GTD used herein. I would especially like to thank Professor Bill Davis for taking the time to go through most of the theory with me and for his comments on the grammatical problems that occured.

<div align="right">Bruce A. Thieman</div>

Contents

List of Figures

List of Tables

Abstract

Using the Geometrical Theory of Diffraction (GTD) the fields due to a monopole array mounted on an aircraft near the top or bottom were analyzed. The aircraft was modeled in its most basic form; an infinitely long elliptical cylinder. The aircraft cross-section at the location of the antenna was modeled as a 2 meter by 4 meter ellipse. The frequency band of operation was 250 mHz to 400 mHz with an average wavelength assumed of 1 meter. The three element array was found to have a beam broadening effect when compared to the array mounted on an infinite ground plane. The array exhibited a poor potential to form a single major lobe in its antenna pattern but had a high mobility of pattern nulls.

ANALYSIS OF ANTENNA ARRAYS ON CYLINDERS

BY THE

GEOMETRICAL THEORY OF DIFFRACTION

I. Introduction

One of the principal problems in the design of a reliable airborne antenna is the effect on volumetric antenna radiation patterns by the aircraft not acting as a flat ground plane. The particular antenna pattern problem to be considered here consists of an antenna array of quarter-wavelength, radial monopoles, which operate in the 250 mHz to 400 mHz range, mounted on an aircraft fuselage near the top or bottom. The array configuration is depicted in Fig. 1.
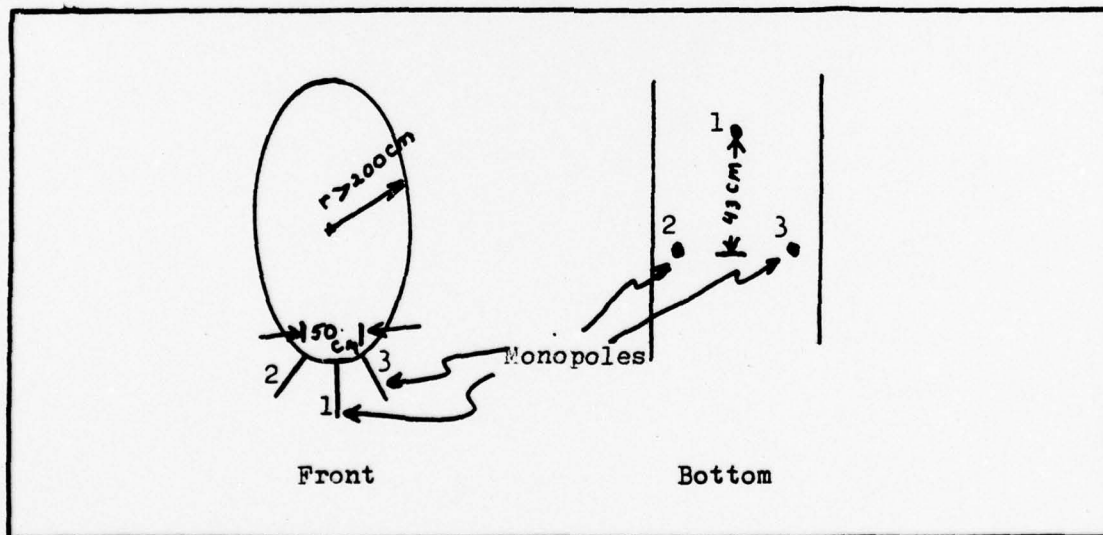
Fig. 1. Array Configuration

Since this is a general analysis, the aircraft is modeled in its most basic form. The fuselage is assumed to be an infinitely long perfectly conducting elliptical cylinder. The cylinder

1

solution employed in this analysis, when compared to the experimental case of one monopole on a cylinder, gives an accuracy of about ±1 dB in pattern computation down to a level about 20 dB below the pattern maximum.

Antenna location on an aircraft is usually based primarily upon convenience with respect to the aircraft structure with no regard for system requirements. The antenna system performance is determined by analyzing antenna patterns of scale models. This approach to antenna design and location requires large amounts of engineering time and money. This investigation develops an analytic approach to determining the antenna system performance.

The first analytic solutions used to determine on-aircraft antenna patterns were the cylindrical harmonic solutions for infinitely long circular (Ref 1; Ref 2) and elliptic cylinders (Ref 3). These solutions modeled the fuselage by a cylinder whose elliptical cross-section approximated the fuselage cross-section at the antenna location. These solutions failed for structures of many wavelengths in diameter unless expanded asymptotically for large dimensions. The expansion of these solutions required computers of very large memory.

A more recent approach is the use of the integral equation method via moment methods. By solving the boundary value problem for fields on aircraft structures, the surface currents and the resulting scattered fields can be found. Richmond (Ref 4; Ref 5), developed a moment solution based on a wire grid modelling structure. This solution required the determination of approximately 100 unknown currents per square wavelength in order that the grid

2

adequately simulate a perfectly conducting surface.

Another approach is the surface current model method (Ref 6).
This method divides the surface of a conducting body into patches,
with each patch having two orthogonal unknown complex currents.
This reduces the number of unknown currents to about 20 per square
wavelength allowing solutions for much larger surfaces. This solu-
tion, modal solution, and the moment method are restricted to lower
frequencies due to the limitation of the size of matrices which
modern computers can solve without unacceptable loss of accuracy.

Another approach that has obtained success at analyzing on-
aircraft antennas is the Geometrical Theory of Diffraction (referred
to simply as the GTD henceforth). The GTD is a high frequency
solution which is divided into two basic problems; wedge diffraction
and curved surface diffraction. Both of these diffraction solutions
have been applied in computing the patterns of slot antennas mounted
on cylinders (Ref 7; Ref 8; Ref 9), rockets (Ref 10), and aircraft
(Ref 11; Ref 12). Using this approach, one applies a ray optics
technique to determine components of the field incident on the
various scatterers. Components of the diffracted field are found
using the GTD solutions in terms of rays which are summed with the
geometrical optics terms in the far field.

The approach applied in this thesis is based on previous work
by Burnside (Ref 13) and Yu (Ref 14), which demonstrated the capa-
bility of the numerical solutions to predict the radiation patterns
of fuselage mounted antennas in an efficient and economical way. If
the volumetric patterns were found directly by analyzing rays on
complex three-dimensional surfaces as done in Reference 12, the

3

resulting numerical solution would be very complex, time-consuming, and uneconomical. Nervertheless, if certain assumptions can be made, the approach undertaken previously can be used to overcome these difficulties and simplify the problem a great deal.

The basic theoretical background on the geometrical theory of diffraction (GTD) for curved surface diffraction is presented in Chapter II. Expressions for the parameters and special functions involved are given in Chapter III. The equation for diffraction by a monopole on an infinitely long cylinder are presented in Chapter III, as is the mathematical model of the aircraft. In Chapter IV, the numerical results obtained for the single monopole case are compared with published results and measurements and in addition the field patterns of the three element array for different phases are presented. Chapter V contains the conclusions.

II. Theoretical Background

For scattering objects that are large in terms of the wavelength,
such as for electrically large aircraft, the GTD is the optimum
approach. The following developement of the GTD assumes; that ray
trajectories are determined by the generalized Fermat's principle,
that the field amplitude variation along a ray path can be found
from power conservation in a tube (or strip) of rays, and that the
diffraction and excitation of waves can be treated as local
phenomena. The validity of these assumptions and the GTD have been
established in published materials.

According to geometrical optics the region exterior to a per-
fectly-conducting surface with a radial electric current source at
point O is divided into an illuminated region and a shadow region
by a plane tangent to the surface at Q_1 called the shadow boundary.
A portion of these two regions adjacent to the shadow boundary is a
transition region. The angular extent of the transition region is
of the order $(k\rho_g)^{-1/3}$ when the source is on the surface; ρ_g being
the radius of curvature of the surface at Q in the direction of
propagation, and k being the wave number $2\pi/\lambda$. The three regions
are depicted in Fig. 2. To solve for the fields due to the array,
the derivation of the high-frequency, far-zone field due to a point
source has to be determined for these three regions.

Diffraction by a Curved Surface

When an incident ray strikes a smooth, curved perfectly con-

5
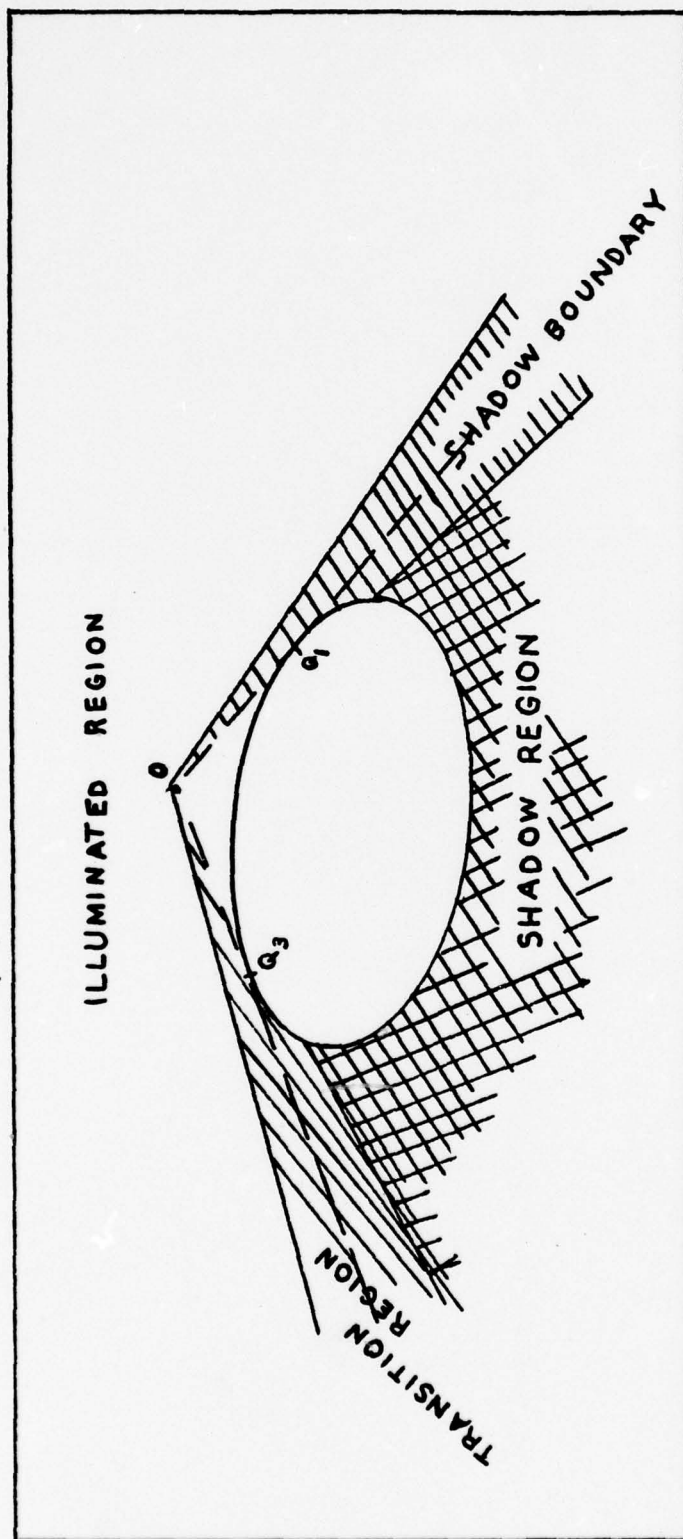
Fig. 2. Point source near a curved surface showing the different regions of radiation

6

ducting surface at grazing incidence, i.e., at the shadow boundary, a part of its energy is diffracted into the shadow region. This phenomena is described by a class of diffracted rays now know as creeping waves (Ref 15). These ray paths include the points Q_1 and Q_2 which form a curve on the diffracting surface, as illustrated in Fig. 3. The actual concept of creeping waves was introduced by Franz and Depperman (Ref 16; Ref 17). The basic concepts, as presented in the following discussion is taken in part form "Asymptotic High-Frequency Methods" by Kouyoumjian (Ref 18).

The diffraction by a smooth curved surface is shown in Fig. 3 in which O is the source point and P is the observation point in the shadow region. Diffracted rays are characterized by an extended form of Fermat's principal which is: The diffracted rays connecting two points O and P in the exterior of a perfectly conducting body are those curves joining O and P which have stationary (optical) length among all curves from O to P having an arc on the body surface. Applying this principle, the line OQ_1Q_2P is the shortest distance between O and P which does not penetrate the surface. In detail, a ray incident on the shadow boundary at Q_1 divides; one part of the incident energy continues straight on as predicted by geometrical optics, a second part follows the surface S into the shadow region as a surface ray shedding diffracted rays tangentially as it propagates where $\hat{t}$, $\hat{n}$, and $\hat{b}$ are the unit vectors in the direction of incidence, normal to the surface S and binormal to the surfave ($\hat{b} = \hat{t} \times \hat{n}$). The incident field $\bar{E}^i(Q_1)$ may be seperated into its normal and binormal components ($\hat{n} \cdot \bar{E}^i(Q_1)$ and $\hat{b} \cdot \bar{E}^i(Q_1)$). It is assumed that these two components induce surface ray fields

7

TOP VIEW

SHADOW BOUNDARY

GEODESICS

Q_1

O

$d\eta_1$

$\hat{b}_1$

Q_2 $\leftarrow d\eta_2$ CAUSTIC

P

$\hat{b}_2$ WAVEFRONT

SIDE VIEW

SHADOW BOUNDARY

CAUSTIC

$\hat{n}_1$ $\hat{t}_1$

Q_1 SURFACE RAY

ρ_c

SHADOW REGION

$\hat{n}_2$

Q_2

$\hat{t}_2$

O INCIDENT RAYS

DIFFRACTING SURFACE

S WAVEFRONT

DIFFRACTED RAY

P
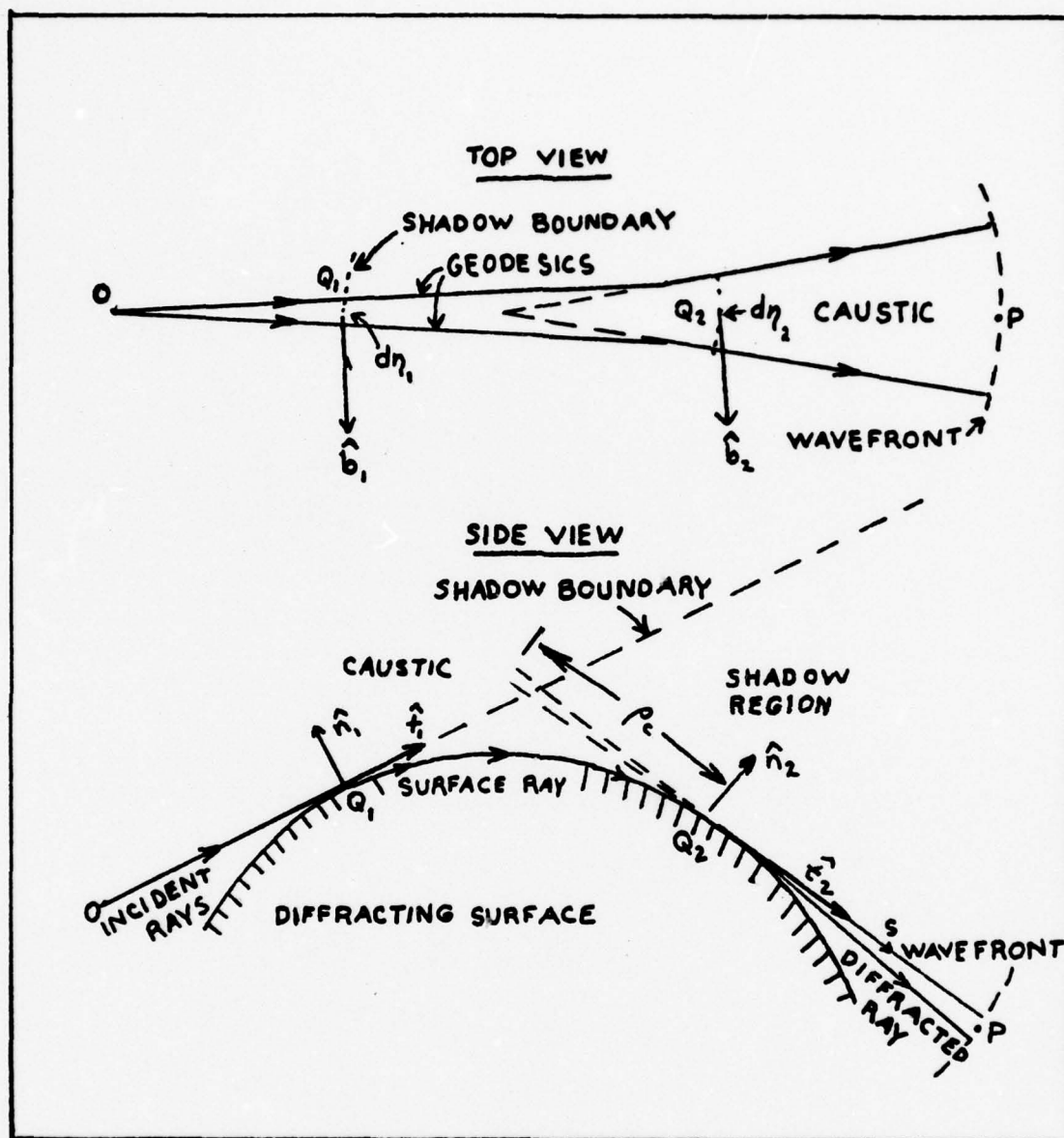
Fig. 3. Diffraction by a smooth convex surface

8

which propagate independently of each other along the geodesic arc between Q_1 and Q_2.

The binormal surface ray field at Q_1 is related to the binormal component of the incident field at Q_1 by

$$A(Q_1)\exp(j\phi(Q_1)) = D^s(Q_1)(\hat{b}_1 \cdot \bar{E}^i(Q_1)) \tag{1}$$

where $D^s(Q_1)$ is the scalar diffraction coefficient for a soft boundary condition. The terms hard and soft boundary conditions are terms from acoustics. A soft boundary is one where the preasure field is zero at the boundary ($\bar{E} = E_z\hat{z}$). A hard boundary condition is one in which the derivative in the direction normal to the boundary is zero ($\partial\bar{E}/\partial n = 0$; $\bar{H} = H_z\hat{z}$).

The amplitude of the surface ray is assumed to be governed by the conservation of energy between a pair of adjacent surface rays. This principal states that in time harmonic fields, the energy flux is the same through every cross section of a tube of rays, such as the astigmatic tube of rays in Fig. 4.
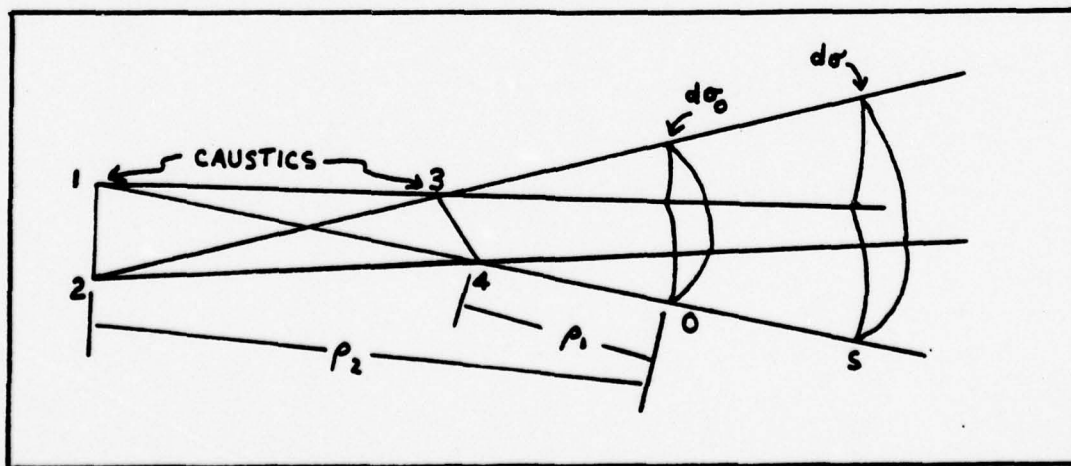
Fig. 4. Astigmatic Bundle of Rays

Let A^2 be the intensity of the field at S and A_o^2, the intensity at the reference point O. For an isotropic, homogeneous medium

$$A^2 d\sigma = A_o^2 d\sigma_o \qquad (2)$$

where $d\sigma$ is the cross section of the tube of rays at S and $d\sigma_o$ is the cross section at O. Therefore

$$A = A_o \sqrt{d\sigma_o / d\sigma} \qquad (3)$$

If s is the distance from O to S, then

$$\frac{d\sigma_o}{d\sigma} = \frac{\rho_1 \rho_2}{(\rho_1 + s)(\rho_2 + s)} \qquad (4)$$

where ρ_1 and ρ_2 are the principal radii of curvature of the wavefront through O.

Applying the energy conservation principle to a narrow strip of rays on a curved surface (see Fig. 5) gives

$$A^2(\ell + d\ell) d\eta(\ell + d\ell) - A^2(\ell) d\eta(\ell) = -2\alpha(\ell) A^2(\ell) d\eta(\ell) d\ell \qquad (5)$$

where $2\alpha(\ell)$ is a proportionality factor relating the change of flux to the energy radiated. Dividing by $d\ell$ and letting $d\ell$ tend to zero gives

$$\frac{d}{d\ell}(A^2 d\eta) = -2\alpha(A^2 d\eta) \qquad (6)$$

10
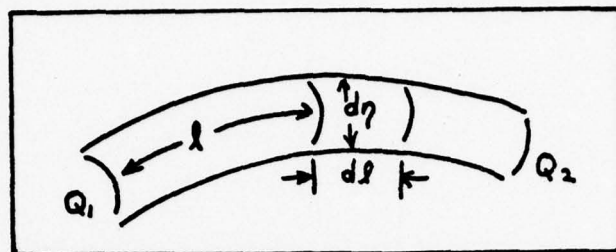
Fig. 5.   A Band of Diffracted Rays
on the Surface of a Diffracting Object

Upon integrating Eq. 6, the result is

$$A(Q_2) = A(Q_1) \sqrt{\frac{d\eta_1}{d\eta_2}} \exp\left[-\int_{Q_1}^{Q_2} \alpha(\ell) d\ell\right] \tag{7}$$

where $d\eta_1$ and $d\eta_2$ = the seperation between a pair of rays at Q_1 and

Q_2 respectively.

$\alpha(\ell)$ = the attenuation constant which is a function of

ℓ and the coordinates along the surface and de-

pends on the local radius of curvature and its

derivatives.

From Fig. 3, Q_2 is a caustic of the diffracted field and the second coustic is located a distance ρ from Q_2. The caustic of a given family of rays is defined as that surface or curve which is everywhere tangent to the ray surface. Thus the surface of a diffracting body is a caustic of the family of diffracted rays resulting from a given field being incident on the body. Thus the binormal component of the diffracted field which radiates from Q_2 towards P can be found using a caustic at Q_2 for a reference point as

$$\hat{b}_2 \cdot \bar{E}^d(P) = D^s(Q_2) A(Q_2) \exp(j\phi Q_2) \sqrt{\frac{\rho}{s(\rho + s)}} \exp(-jks) \tag{8}$$

11

where $D^s(Q_2)$ is a diffraction coefficient of the soft boundary. Based on the reciprocity principle--that a source at O produces the same field at P as a source at P produces at O--$D^s(Q_2)$ has the same form as $D^s(Q_1)$. Combining Eqs. (1), (7), and (8) yields

$$\hat{b}_2 \cdot \bar{E}^d(P) = (\hat{b}_1 \cdot \bar{E}^i(Q_1))D^2(Q_1)D^s(Q_2)\sqrt{\frac{d\eta_1}{d\eta_2}}\sqrt{\frac{\rho}{s(\rho + s)}}$$

$$\cdot \exp\left[-jk(\ell + s) - \int_{Q_1}^{Q_2}\alpha^s(\ell)d\ell\right] \tag{9}$$

The incident field $\hat{b}_1 \cdot \bar{E}^i(Q_1)$ excites an infinity of surface ray modes, each with its own diffraction coefficient and attenuation coefficient. For example, in the canonical problem in Appendix A, if the field scattered from a cylinder given by Eq. (58) is approximated asymptotically, it is seen that there is a surface ray mode associated with each term of the series, i.e., with each value of m. Therefore, Eq. (9) is replaced by

$$\hat{b}_2 \cdot \bar{E}^d(P) = (\hat{b}_1 \cdot \bar{E}^i(Q_1))\sqrt{\frac{d\eta_1}{d\eta_2}}\sqrt{\frac{\rho}{s(\rho + s)}}\exp(-jk(\ell + s))$$

$$\cdot \sum_{m=1}^{\infty}D_m^s(Q_1)D_m^s(Q_2)\exp\left[-\int_{Q_1}^{Q_2}\alpha_m^s(\ell)d\ell\right] \tag{10}$$

This equation relates the diffracted field at P to the incident field at Q_1 for the soft boundary condition.

An expression similar to Eq. (10) is also obtained for the normal component of the incident field:

12

$$\hat{n}_2 \cdot \bar{E}^d(P) = (\hat{n}_1 \cdot \bar{E}^i(Q_1)) \sqrt{\frac{d\eta_1}{d\eta_2}} \sqrt{\frac{\rho}{s(\rho + s)}} \exp(-jk(\ell + s))$$

$$\cdot \sum_{m=1}^{\infty} D_m^h(Q_1) D_m^h(Q_2) \exp\left[-\int_{Q_1}^{Q_2} \alpha_m^s(\ell) d\ell\right] \tag{11}$$

In this case, the scalar diffraction coefficients and attenuation constants for the hard surface diffraction replace those of the soft surface. The vector diffracted field at P can now be written in terms of the electromagnetic field incident at Q_1 as

$$\bar{E}(P) = (\hat{n}_2\hat{n}_1 v(Q_1,Q_2) + \hat{b}_2\hat{b}_1 u(Q_1,Q_2)) \cdot \bar{E}^i(Q_1) \sqrt{\frac{\rho}{s(\rho + s)}} \exp(-jks) \tag{12}$$

where $v(Q_1,Q_2)$ and $u(Q_1,Q_2)$ are equal to

$$\frac{d\eta_1}{d\eta_2} \exp(-jk\ell) \sum_{m=1}^{\infty} D_m(Q_1) D_m(Q_2) \exp\left[-\int_{Q_1}^{Q_2} \alpha_m(\ell) d\ell\right] \tag{13}$$

with the superscripts h and s, respectively added to D_m and α_m. The $d\eta_1$, $d\eta_2$ and ρ are found by differential geometry involving the rays and surface; this is discussed at length in Levy and Keller (Ref 15).

To obtain the diffraction and attenuation constants, the exact canonical solution of the boundary value problem for the diffraction in question must be known. Such a solution is expanded asymptotically for ka large where a is the radius of curvature for cylindrical diffraction. By comparing this expansion with the GTD solution, the values of α_m and D_m can be determined. Appendix A contains a derivation of the generalized diffraction coefficient

13

and attenuation coefficient for diffraction by curved surfaces.

The diffraction thus far discussed is applied to an open curved surface. For a closed surface, each surface ray mode produced at Q_1 encircles the surface an infinite number of times. The length of the surface ray path for the nth encirclement is $\ell + nT$ where T is the distance traveled in one transversal of the closed surface. These multiple encircling rays may be summed to contribute

$$1 - \exp\left[-jkT - \int_0^T \alpha_m(\ell)d\ell\right] \tag{14}$$

to the denominator of the diffracted field. Note for this derivation that the $\exp(jkz)$ convention has been adopted.

Direct Rays

The rays emanating from a point current element with current moment $I\Delta x$ determines the incident field for the diffracted and reflected rays as well as the field at all points where Fermat's principle produces a straight line from the source.

Referring to Fig. 6, A is defined as (Ref 19: 16)

$$A_x = \frac{I_o\Delta x \, \exp(-jks')}{4\pi s'} \tag{15}$$

Applying Maxwell's equations

$$\overline{H} = \nabla \times A_x\hat{x} = \nabla A_x \times \hat{x} \tag{16}$$

$$= \frac{I\Delta x}{4\pi} \nabla \frac{\exp(-jks')}{s'} \times \hat{x} \tag{17}$$

14

$$\bar{H} = \frac{I\Delta x}{4\pi}\left[-jk\frac{(\exp(-jks'))}{s'} - \frac{1}{s'^2}\exp(-jks')\right]\hat{r} \times \hat{x} \qquad (18)$$
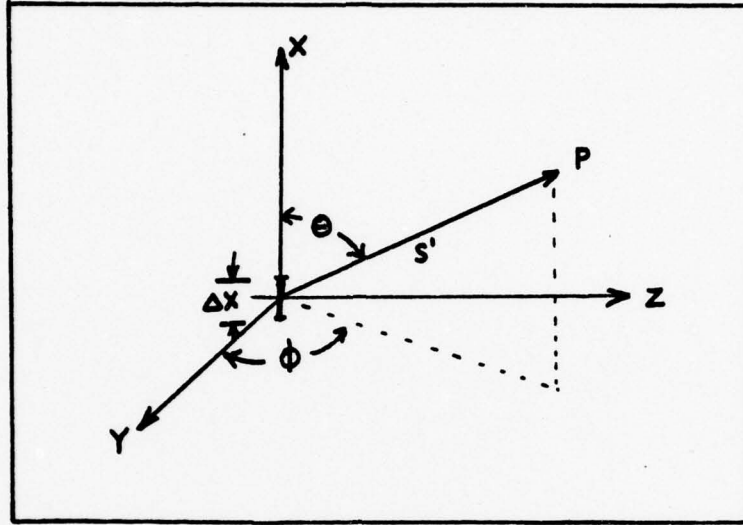
Fig. 6. Geometry for current source at origin

Since

$$\hat{r} \times \hat{x} = \hat{r} \times (\hat{r}\cos\theta - \hat{\theta}\sin\theta) = -\hat{\phi}\sin\theta \qquad (19)$$

then

$$\bar{H} = \frac{I\Delta x}{4\pi}\left[\frac{jk}{s'} + \frac{1}{s'^2}\right]\exp(-jks')\sin\theta\,\hat{\phi} \qquad (20)$$

In the far zone field the $1/s'$ term is dominant, the $1/s'^2$ term tending to zero much faster than $1/s'$ therefore it can be neglected.

The electric field is obtained from

$$\bar{E} = \frac{1}{j\omega\epsilon}\nabla \times \bar{H} \qquad (21)$$

, to give

$$\bar{E} = \frac{I\Delta x}{4\pi}\exp(-jks')\left[\frac{j\omega\mu}{s'} + \sqrt{\frac{\mu}{\epsilon}}\frac{1}{s'^2}\right]\sin\theta\,\hat{\theta} +$$

$$+ \sqrt{\frac{\mu}{\epsilon}}\left[\frac{\mu}{\epsilon}\frac{1}{s'^2}\right]\cos\theta\,\hat{r} \qquad (22)$$

15

Again, in the far zone field the 1/s' term is dominant and the direct electric field becomes

$$\overline{E} = \frac{I\Delta x}{4\pi} \exp(-jks') \frac{j\omega\mu}{s'} \sin\theta\,\hat{\theta} \tag{23}$$

Launching Coefficients and Constants

The theory presented up to now has assumed a point source near a cylinder. Monopoles mounted on a cylinder could be modeled as a line of point sources with sinusoidally distributed amplitudes, using this theory. The far-zone field would then be the result of vectorially summing the fields from each source point at each field point. The result is a large number of ray tracings and field calculations for even a simple antenna array.

To simplify the calculations, the sum of the incident fields due to all of the point sources making a monopole model are approximated by a launching coefficient. To determine the launching coefficients, the radiation from an axial mounted electric current source on a perfectly conducting cylinder is analyzed. The asymptotic solution of this canonical problem is described in Appendix B, where it is found that

$$L_m^s = -\left(\frac{jk}{2}\right)^{1/2} H_{\nu_m}^{(2)}{}'(ka) D_m^s(Q_1) \tag{23}$$

$$L_m^h = -j\left(\frac{jk}{2}\right)^{1/2} H_{\nu_m}^{(2)}(ka) D_m^h(Q_1)$$

where ν_m are the zeroes of the Hankel function in the first equation and the zeroes of the derivative of the Hankel function in the

16

second equation. Note that Q_1 is now the source location. These launching coefficients are valid for monopoles whose length is small in comparison to the dimensions of the scatterers.

Eq. (12) now becomes

$$\overline{E}(P) = (\hat{n}_2\ v(Q_1,Q_2) + \hat{b}_2\ u(Q_1,Q_2))\sqrt{\frac{\rho}{s(\rho + s)}}\exp(-jks) \qquad (24)$$

where $v(Q_1,Q_2)$ and $u(Q_1,Q_2)$ are equal to

$$\sqrt{\frac{d\eta_1}{d\eta_2}}\exp(-jkl)\sum_{m=0}^{\infty} L_m(Q_1)D_m(Q_2)\exp\left[-\int_0^{Q_2}\alpha_m(\ell)d\ell\right] \qquad (25)$$

with the superscripts h and s, respectively added to D_m, L_m, and α_m.

Diffraction Coefficients and Attenuation Constants

The diffraction coefficients and attenuation constants depend on the local geometry of the surface, the wave number k, and the nature of the surface, as described by the boundary conditions. Voltmer (Ref 20) has derived the diffraction coefficients and attnuation constants for general convex surfaces and are included in Table I. Appendix A contains the derivation of D_m and α_m for a cylinder.

To first order these functions are

$$\alpha_m^s = \frac{1}{\rho_g}\left(\frac{k\rho_g}{2}\right)^{1/3} q_m\exp(j\pi/6) \qquad (26)$$

$$(D_m^s)^2 = \frac{\exp(-j\pi/12)}{2^{5/6}\pi^{1/2}(k\rho_g)^{1/6}} \frac{\rho_g^{1/2}}{(A_i{'}(-q_m))^2} \qquad (27)$$

17

TABLE I

GENERALIZED DIFFRACTION COEFFICIENTS AND ATTENUATION CONSTANTS

Surface	SQUARE OF DIFFRACTION COEFFICIENT $D_m^2 = (\text{Column A}) \cdot (\text{Column B})$		ATTENUATION CONSTANT $q_m = (\text{Column C}) \cdot (\text{Column D})$	
	A. Keller's Result	B. Correction Terms	C. Keller's Result	D. Correction Terms
Soft Acoustic and Soft EM	$\dfrac{e^{-1/2}\,2^{-5/6}\,\rho_g^{1/3}\,e^{-j\pi/12}}{k^{1/6}(Ai'(-q_m))^2}$	$1 + \left(\dfrac{2}{k\rho_g}\right)^{2/3} q_m\left(\dfrac{1}{30} + \dfrac{\rho_g}{4\rho_{tn}} + \ldots\right)e^{-j\pi/3}$	$\dfrac{q_m}{\rho_g}\,e^{-j\pi/6}\left(\dfrac{k\rho_g}{2}\right)^{1/3}$	$1 + \left(\dfrac{2}{k\rho_g}\right)^{2/3} q_m\left(\dfrac{1}{60} - \dfrac{2}{45}\rho_g\dot{\rho}_g + \dfrac{4}{135}\dot{\rho}_g^2\right)e^{-j\pi/3}$
Hard Acoustic		$1 + \left(\dfrac{2}{k\rho_g}\right)^{2/3}\left[\dfrac{1}{q_m}\left(\dfrac{1}{30} + \dfrac{\rho_g}{4\rho_{tn}} + \ldots\right)\right.$ $\left. - \dfrac{1}{10} + \dfrac{\rho_g}{4\rho_{tn}} + \ldots\right]e^{-j\pi/3} - \dfrac{1}{2}\dfrac{\rho_g}{q_m}$	$\dfrac{q_m\,e^{j\pi/6}}{\rho_g}\left(\dfrac{k\rho_g}{2}\right)^{1/3}$	$1 + \left(\dfrac{2}{k\rho_g}\right)^{2/3}\left[\dfrac{1}{q_m}\left(\dfrac{1}{60} - \dfrac{2}{45}\rho_g\dot{\rho}_g + \dfrac{4}{135}\dot{\rho}_g^2\right)\right.$ $\left. + \left(\dfrac{1}{10} + \dfrac{\rho_g}{4\rho_{tn}} - \dfrac{\rho_g\dot{\rho}_g}{60} + \dfrac{\dot{\rho}_g^2}{90}\right)\right]e^{-j\pi/3} - \dfrac{1}{2}\dfrac{\rho_g}{q_m}$
Hard EM	$\dfrac{e^{-1/2}\,2^{-5/6}\,\rho_g^{1/3}\,e^{-j\pi/12}}{k^{1/6}\overline{q_m}(Ai(-\overline{q_m}))^2}$	$1 + \left(\dfrac{2}{k\rho_g}\right)^{2/3}\left(\dfrac{1}{q_m}\left(\dfrac{1}{30} - \dfrac{\rho_g}{4\rho_{tn}} + \ldots\right)\right.$ $\left. - \dfrac{1}{10} - \dfrac{\rho_g}{4\rho_{tn}} + \ldots\right)e^{-j\pi/3} - \dfrac{1}{2}\dfrac{\rho_g}{q_m}$		$1 + \left(\dfrac{2}{5\rho_g}\right)^{2/3}\left(\dfrac{1}{q_m}\left(\dfrac{1}{60} - \dfrac{2}{45}\rho_g\dot{\rho}_g + \dfrac{4}{135}\dot{\rho}_g^2\right)\right.$ $\left. + \left(\dfrac{1}{10} - \dfrac{\rho_g}{4\rho_{tn}} - \dfrac{\rho_g\dot{\rho}_g}{60} + \dfrac{\dot{\rho}_g^2}{90}\right)\right)e^{-j\pi/3} + \dfrac{1}{2}\dfrac{\rho_g}{q_m}$

ρ_g = radius of curvature along the geodesic

ρ_{tn} = radius of curvature perpendicular to the geodesic (transverse curve)

Dots indicate differentiation with respect to arc length variable

18

for the "soft" surface, where ρ_g is the radius of curvature of the surface along which the surface ray is propagating in the plane containing the normal and tangent to the surface ray, and

$$\alpha_m^h = \frac{1}{\rho_g}\left(\frac{k\rho_g}{2}\right)^{1/3} \bar{q}_m \exp(j\pi/6) \tag{28}$$

$$(D_m^h)^2 = \frac{\exp(-j\pi/12)}{2^{5/6}\pi^{1/2}(k\rho_g)^{1/6}\bar{q}_m} \frac{\rho_g^{1/2}}{(A_i(-\bar{q}_m))^2} \tag{29}$$

for the hard surface, where the Miller-type Airy function is given by

$$A_i(-x) = \frac{1}{\pi}\int_0^\infty \cos(\tfrac{1}{3}t^3 - xt)dt \tag{30}$$

$$A_i(-q_m) = 0 \tag{31}$$

$$A_i'(-\bar{q}_m) = 0 \tag{32}$$

where q_m and $\bar{q}_m$ are the zeroes of A_i and A_i' respectively with the prime denoting differentiating with respect to the argument of the function. These zeroes are calculated in Appendix C.

The terms "hard" and "soft" refer to the boundary conditions. A soft boundary condition is a Direchlet boundary (the field vanishes at the surface). A hard boundary is a Neumann boundary condition (the normal derivative of the field vanishes at the surface). This assumes two types of surface ray modes; one in which $\bar{E} = \hat{b}E$, satisfying a soft boundary condition, and one in which $\bar{E} = \hat{n}E$, satisfying the hard boundary condition. The corresponding coefficient approximations are essentially what Keller and Levy (Ref 15:166-169) derived. Table I contains Voltmer's

19

corrected results.

Transition Regions

The series representations are rapidly convergent when the field point is deep in the shadow region. When the local average radius of curvature of the surface is larger than a wavelength at the points of diffraction, only the 1st terms are neccessary to achieve good accuracy. As the field diffraction point Q_2 approaches Q_1 (i.e. l becomes very small), more terms must be added to maintain accuracy and it becomes inconvenient to treat the excitation, propagation and diffraction of the surface ray seperately. The series representation can now be approximated by integral representations, which have been found to be proportional to Fock type functions. When the source is on the surface, the angular extent of the transition region from the shadow boundary is nearly $(k\rho_g)^{-1/3}$ radians. The expressions for the fields in the transition region are also deduced from the asymptotic solutions to appropriate canonical problems as described in Appendix E.

The well tabulated Fock functions (Ref 21) are

1) Hard Fock function

$$g(\xi) = \frac{1}{\sqrt{\pi}} \int_{\Gamma_1} \frac{\exp(-j\tau\xi)}{w_2'(\tau)} d\tau \tag{33}$$

2) Soft Fock function

$$\tilde{g}(\xi) = \frac{1}{\sqrt{\pi}} \int_{\Gamma_1} \frac{\exp(-j\tau\xi)}{w_2(\tau)} d\tau \tag{34}$$

which are described in Appendix E and tabulated in Appendix G. The argument of the Fock function to the first order is

$$\xi = \int_{Q_1}^{Q_2} \frac{1}{\rho_g}\left(\frac{k\rho_g}{2}\right)^{1/3} d\ell \qquad (35)$$

When the field point is in the shadow region, $\ell > 0$ and when the field point is in the illuminated portion of the transition region, $\ell < 0$, where ℓ is the distance traveled on the surface of the cylinder. Note that for these expressions that the surface ray divergence factor $d\eta_1/d\eta_2$ is equal to one in this region.

In the transition region, for sources very close to the surface the term

$$\sum_{m=1}^{\infty} L_m^h(Q_1) D_2^h(Q_2) \exp\left[-\int_{Q_1}^{Q_2} \alpha_m(\ell) d\ell\right] \qquad (36)$$

in Eq. (25) is replaced for $v(Q_1,Q_2)$ by

$$\begin{cases} g(\xi), & \ell \leq 0 \\ g(\xi)\delta, & \ell \geq 0 \end{cases} \qquad (37)$$

and for $u(Q_1,Q_2)$ by

$$\begin{cases} j(\hat{n}_1 \cdot \hat{s}/\xi)g(\xi), & \ell \leq 0 \\ -jg(\xi)\delta/m, & \ell \geq 0 \end{cases} \qquad (38)$$

where

$$m = \left(\frac{k\rho_g(Q_1)}{2}\right)^{1/3} \qquad (38)$$

$$\delta = (\rho_g(Q_2)/\rho_g(Q_1))^{1/6} \qquad (39)$$

21

III. Diffraction by an
Infinitely Long Elliptic Cylinder

The special case of the GTD solution treated here is one in
which $1/4\lambda$ monopole antennas are mounted on the curved surface of
an infinitely long, 2λ by 4λ elliptical cylinder. An average
wavelength of 1 meter is assumed for this problem.

The particular array to be considered is depicted in Fig. 1.
To solve the field problem, each monopole is approximated by a
launch coefficient. The field at the field point P will be the
sum of the fields produced by each source.

Ray Approximations

Previous work by Pathak and Luebbers (Ref 22) has shown that
in the illuminated region (P_1, see Fig. 7), the diffracted rays s_1
and s_2 have a negligable amplitude compared to the direct ray s_0.
For point sources on the cylinder, the field can be modeled as
only ray s_0 and Eq. (23).

In the shadow region only the diffracted rays s_1 and s_2
contribute to the field at P_3. Since the rays leaving Q_1 (or O)
and encircling the cylinder n times, cover a cylinder circumference
of about nine meters, they are heavily attenuated and their effect
is very small. The field at P_3 is then the sum of the rays $Q_1 Q_2 P_3$
and $Q_1 Q_3 P_3$ applied to Eq. (24).

In the transition region, the integral form in Eq. (36) and
(37) are used to solve for the field at P_2, again simplified by
ignoring those rays which encircle the cylinder one or more times.
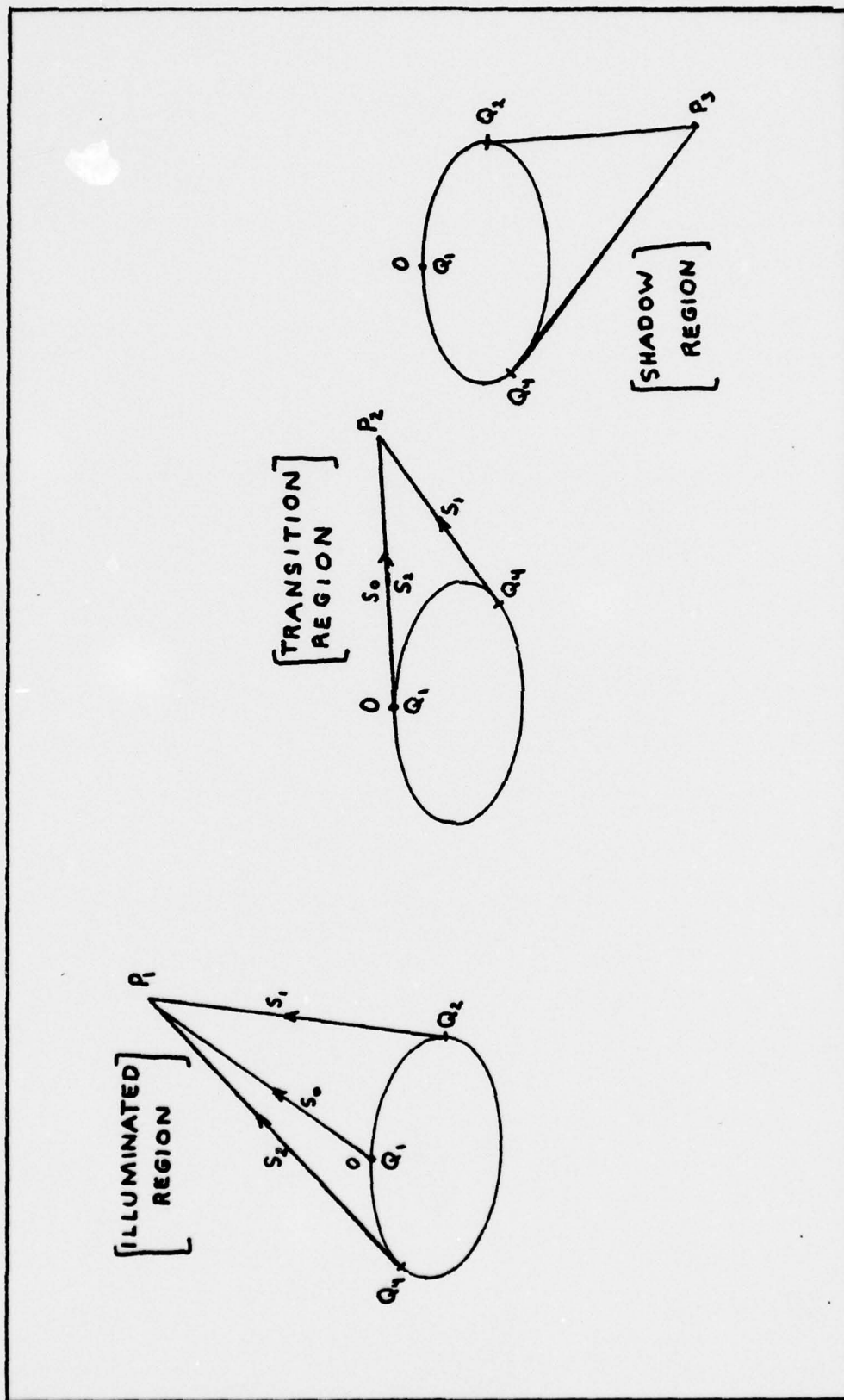
Fig 7. Rays Emanating From A Source On A Curved Surface

Note that for s_1 the diffraction field formula in Eq. (23) is used. For the equations in all of these regions, the spread factor $d\eta_1/d\eta_2$ is one.

Field Equations

The GTD solutions for the radiated electric field of a point source on an elliptical cylinder, as shown in Fig. 8, with all amplitudes combined into A and neglecting torsional effects are

Lit Region

$$E = -A \sin(\Theta_m)\exp(-j(ks' + \varphi)\hat{\theta} \tag{40}$$

Transition Region

    a) Lit side

$$E = \frac{A}{2}\sin(\Theta_m)\exp\left[-j(k(s - \ell) + \varphi\right]g^*(-\xi) \tag{41}$$

    b) Shadow side

$$E = \frac{A}{2}\exp\left[-j(k(s + \ell) + \varphi)\right]g^*(\xi)\left(\frac{\rho_g(Q_2)}{\rho_g(Q_1)}\right)^{1/6}\hat{n} \tag{42}$$

Deep Shadow Region

$$E = \sum_j A \exp\left[-j(k(s + \ell) + \varphi)\right]\hat{n}_j$$

$$\cdot \sum_{m=1} \exp\left[-\int_{Q_1}^{Q_2}\alpha_m^h(\ell)d\ell\right]L_m^h(Q_1)D_m^h(Q_2) \tag{43}$$

24
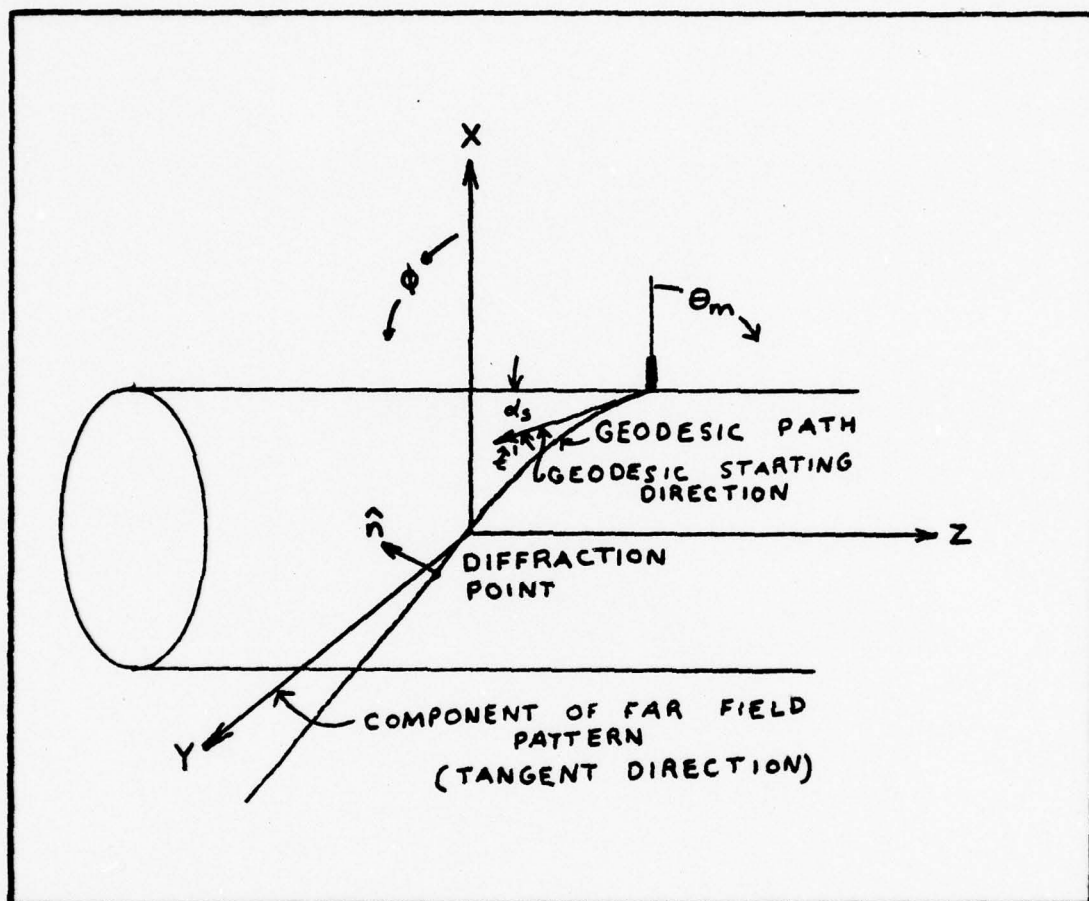
Fig 8. Geometry of monopole antenna mounted on an infinitely
long elliptic cylinder

Where

$g^*(\cdot)$ complex conjugate of the Fock function (Ref 21)

$\hat{n}, \hat{b}, \hat{t}$ normal, binormal and tangent unit vectors to the surface

ρ_g longitudinal radius of curvature

ξ defined in Eq. (35)

φ phase of source

A amplitude of source

s' distance from source to diffraction point or field point if cylinder is not intersected.

s distance from diffraction point Q_2 to field point

Geometry of Elliptical Cylinder (Equations)

In order to analyze this problem by GTD, an efficient solution for the geodesic paths on the elliptic cylinder must be found. The coordinate system adopted here is illustrated in Fig. 9 and defined by

$$x = d \cosh u \cos v = a_f \cos v$$

$$y = d \sinh u \sin v = b_f \sin v$$

$$z = z \tag{44}$$

where 2d is the distance between the foci of the ellipse. To define an ellipse, u must equal $\tanh^{-1}(b_f/a_f)$. The coordinate v then defines any point on the ellipse and varies from 0 to 2π.

Using the calculus of variations, the geodesic paths on an elliptic surface are given by

26

$$z = \frac{C}{\sqrt{1 - C^2}} \int_{v_i}^{v_f} \sqrt{a_f^2 \sin^2 v + b_f^2 \cos^2 v} \, dv \qquad (45)$$

where v_i and v_f are the equivalent of Q_1 and Q_2 respectively in this parametric form.
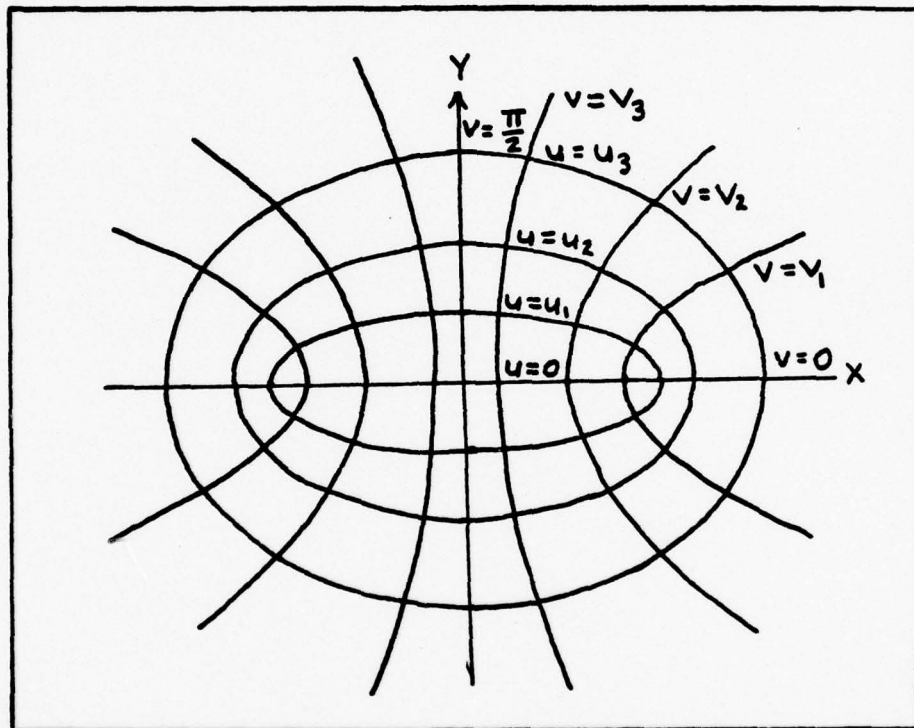
Fig. 9. Elliptic Cylinder Coordinate System (Ref 14:26)

If one defines the geodesic starting direction by the angle (α_s) as shown in Fig. 8, then $C = -\cos \alpha_s$. The parameters of the problem are

$$z = \frac{-\cos \alpha_s}{|\sin \alpha_s|} \int_{v_i}^{v_f} \sqrt{a_f^2 \sin^2 v + b_f^2 \cos^2 v} \, dv \qquad (46)$$

$$\lambda = \frac{1}{\sin\alpha_s} \int_{v_i}^{v_f} \sqrt{a_f^2 \sin^2 v + b_f^2 \cos^2 v} \; dv \qquad (47)$$

(arc length)

$$\hat{e}_1 = \frac{-a_f \sin v \hat{x} + b_f \cos v \hat{y}}{\sqrt{a_f^2 \sin^2 v + b_f^2 \cos^2 v}} \qquad (48)$$

(curvalinear

coordinates)

$$\hat{e}_2 = \hat{z} \qquad (49)$$

$$\hat{t} = \sin\alpha_s \hat{e}_1 - \cos\alpha_s \hat{e}_2 \qquad \text{(unit tangent} \quad (50)$$

vector)

$$\hat{n} = \frac{b_f \cos v \hat{x} + a_f \sin v \hat{y}}{\sqrt{a_f^2 \sin^2 v + b_f^2 \cos^2 v}} \qquad \text{(unit normal} \quad (51)$$

vector)

$$\hat{b} = \hat{t} \times \hat{n} = -\cos\alpha_s \hat{e}_1 - \sin\alpha_s \hat{e}_2 \quad \text{(unit binormal} \quad (52)$$

vector)

$$\rho_g = \frac{(a_f^2 \sin^2 v + b_f^2 \cos^2 v)^{3/2}}{a_f b_f \sin^2 \alpha_s} \qquad (53)$$

(longitudinal

radius of curvature)

Using the preceeding Eqs. (40)-(53), the total radiated field for a point source on a cylinder can be determined.

28

IV. Pattern Calculations

The field equations (40) - (53) are used in the following figures to calculate the field due to the array in Fig. 1. The tabulated fields due to each monopole are included in Appendix G.

To verify the general GTD equations derived for a monopole, the antenna pattern for a single monopole on the cylinder was calculated and compared to experimental results obtained from published literature (Ref 3:662). Fig. 10 contains a plot of both the experimental data and the calculated values. The variation of the experimental field is do to interference from the rays that encircle the cylinder more than once. It was assumed in the calculations that for fields not in the deep shadow region, that only the dominant term would be considered.

Fig. 11 and Fig. 12 (Ref 14:64) provide a means of comparison of the calculated values with those obtained from a scale model test of an aircraft. Fig. 10 and Fig. 11 are almost identical except that the theoretical case exhibits a stronger field in the deep shadow region. The effect of wings (Fig. 12) on the aircraft causes an even further degradation of field strength in the shadow region. The calculated antenna patterns are therefore valid as a good approximation for θ within the range of $\pm 105^\circ$ with respect to the antenna when the antenna is mounted near the top or bottom of the fuselage.

Fig. 13 is a plot of the antenna pattern of antenna 2 or 3. Do to symmetry, their patterns are reflections of each other. The effect of mounting the antenna off of the main axis of the cylinder is to shift the nulls of the pattern as well as cause sharper

changes in the pattern where the minima of the radius of curvature of the cylinder occur. Note that the null has shifted about 26° from its position in Fig. 10 although antenna 2 and 3 are mounted perpendicular to the cylinder surface at a point that is about 14° off of the primary axis of the ellipse ($v_i \sim 14^{\circ}$). This shift is caused by the antenna angle in space being about 26° from the verticle.

Fig. 14 is a plot of the antenna pattern with all three elements of the array driven with the same amplitude and phase. Comparing this pattern to that of a 3-element triangular array depicted in Fig. 15, driven under the same conditions, shows that the cylinder has the effect of broadening the lobes as well as increasing the angle θ where the pattern maxima occurs. The result is a pattern more like that of a single monopole or dipole in space.

Fig. 16 is a plot of the antenna array pattern with element 1 driven 45° out of phase with elements 2 and 3. It takes very little phase change to drastically alter the pattern. The effect of the out of phase element is to focus more of the energy in the lit region of the cylinder. By changing elements 2 or 3 such that they are out of phase with each other should eliminate the null at $\theta = 0$ and also allow the lobes to be moved or combined into a narrower beam as well as move the nulls.
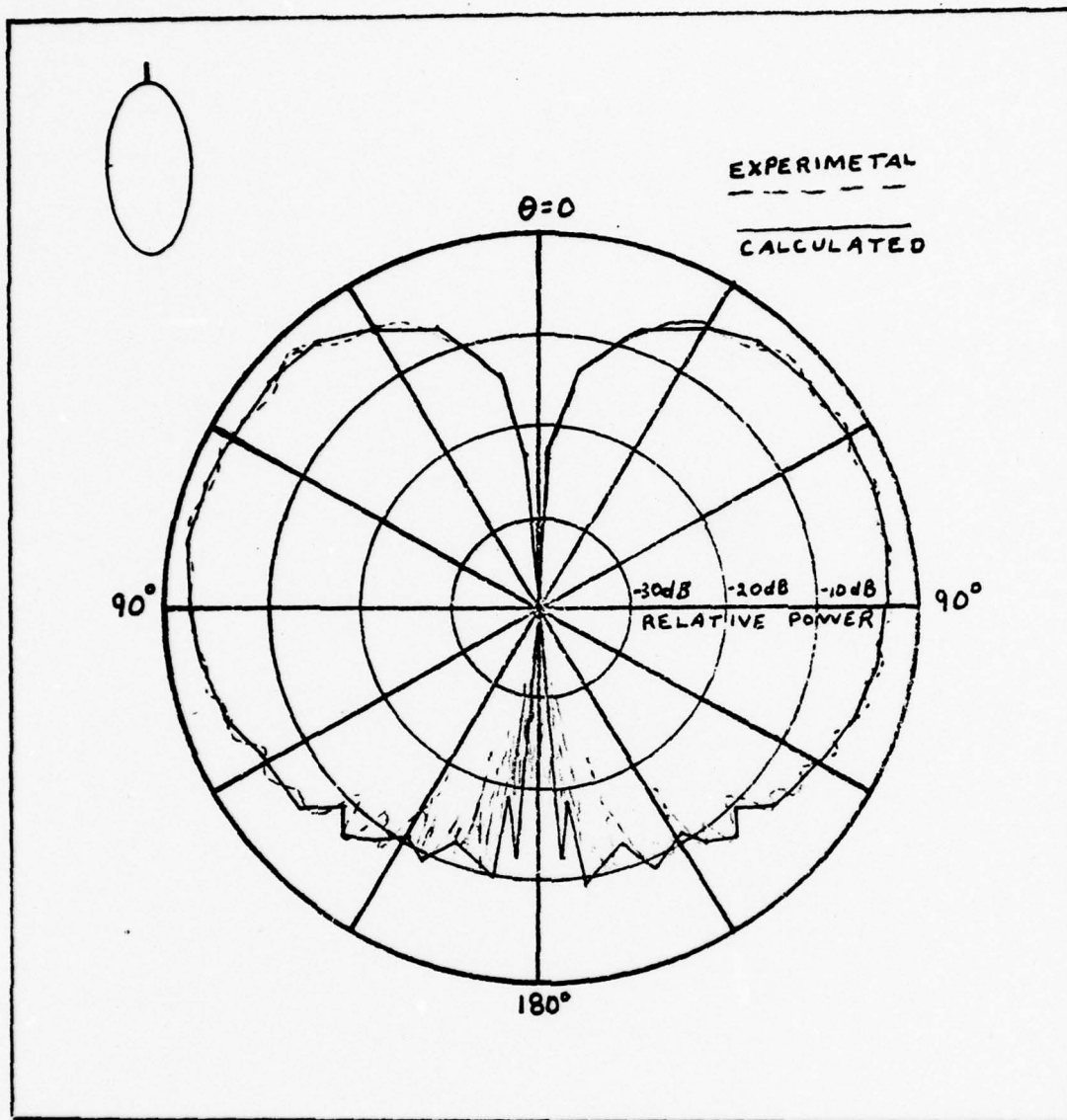
Fig 10. Antenna pattern of monopole on major axis of elliptical cylinder (calculated and experimental)
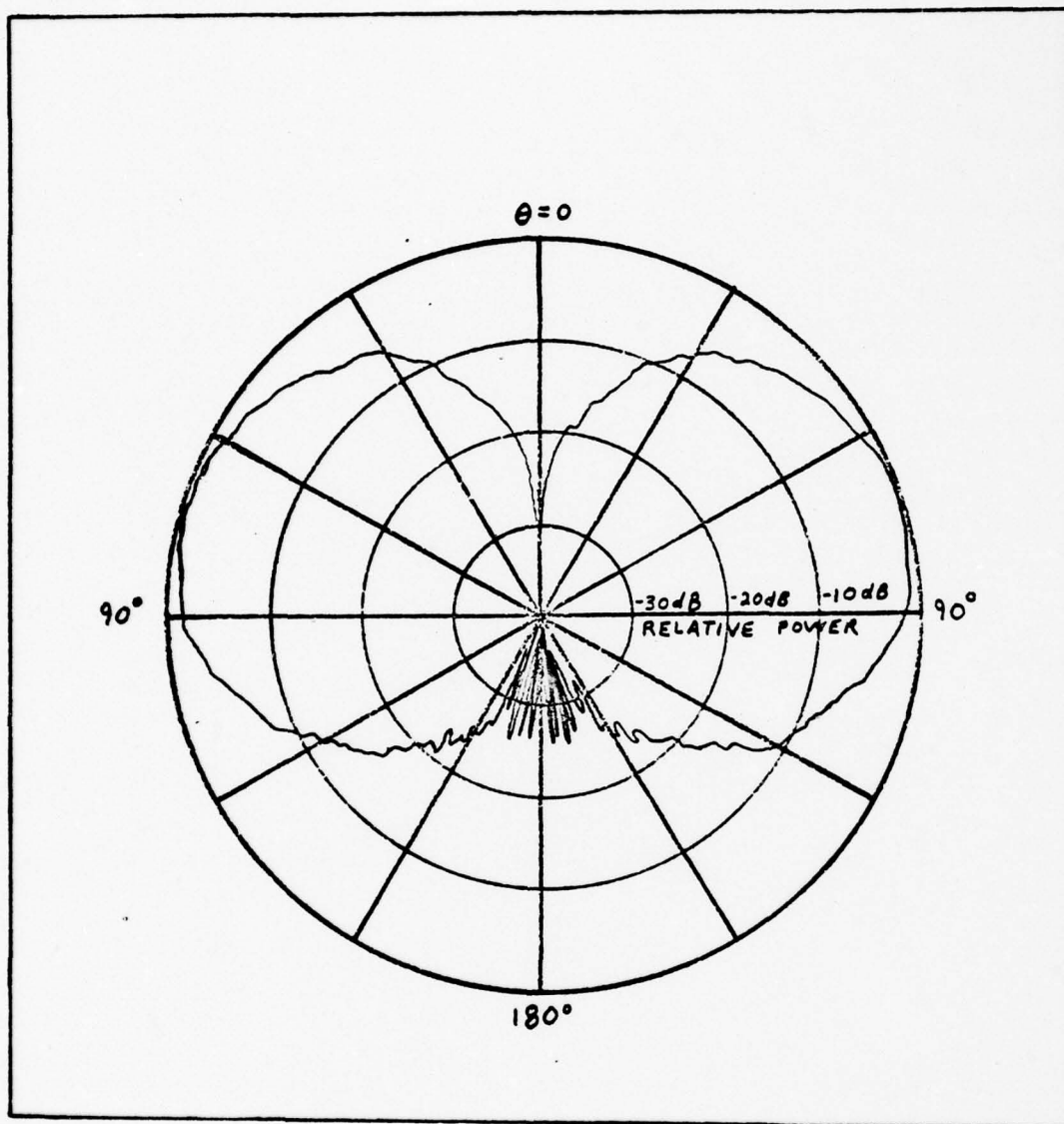
Fig. 11. Roll plane pattern (E_ϕ) for a 1/25 scale model of a KC-135 with a $\lambda/4$ monopole on the fuselage forward of the wings. (from Ref 14:64)
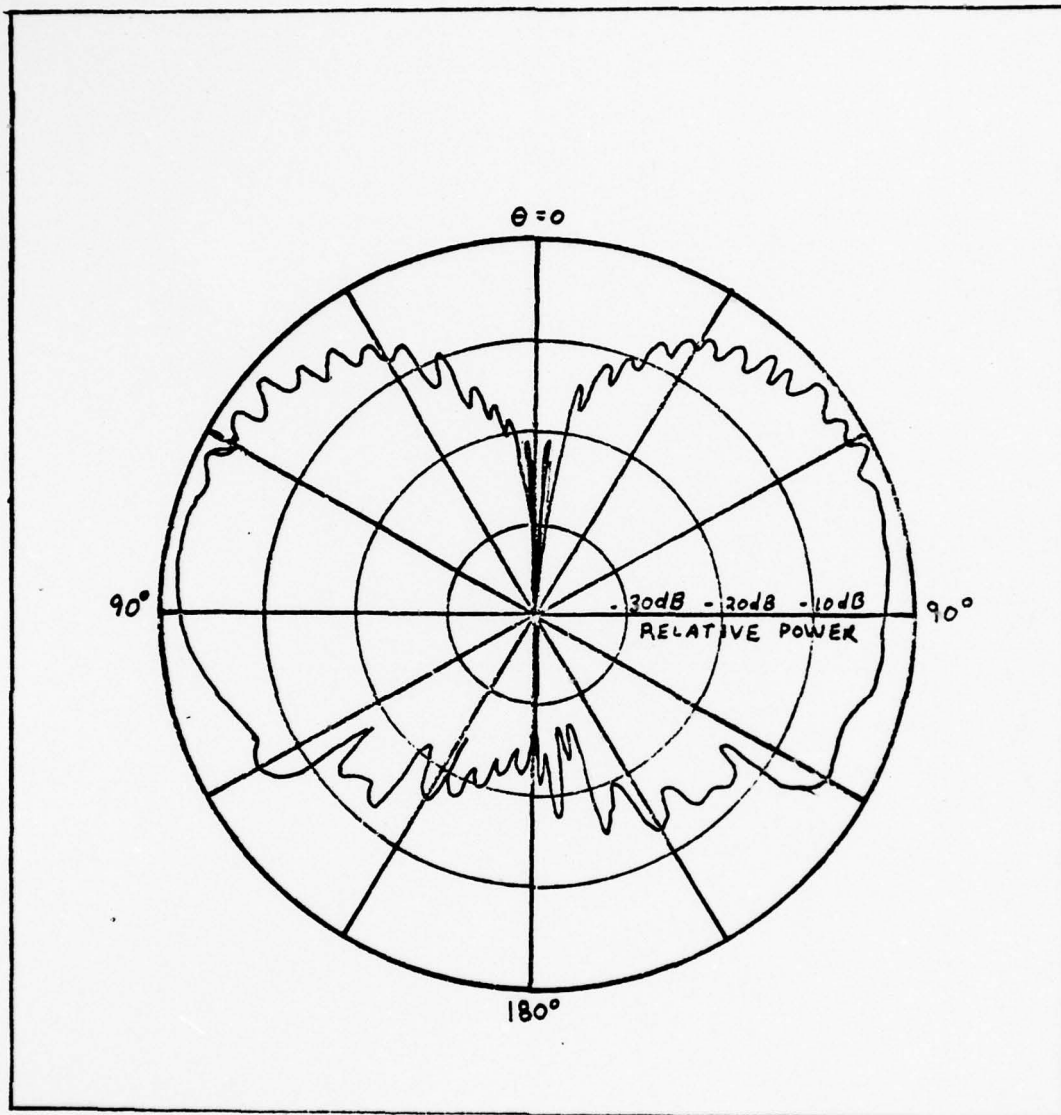
Fig. 12. Roll plane pattern (E$_\phi$) for a $\lambda/4$ monopole
above the wings.(from Ref 12:99)

33
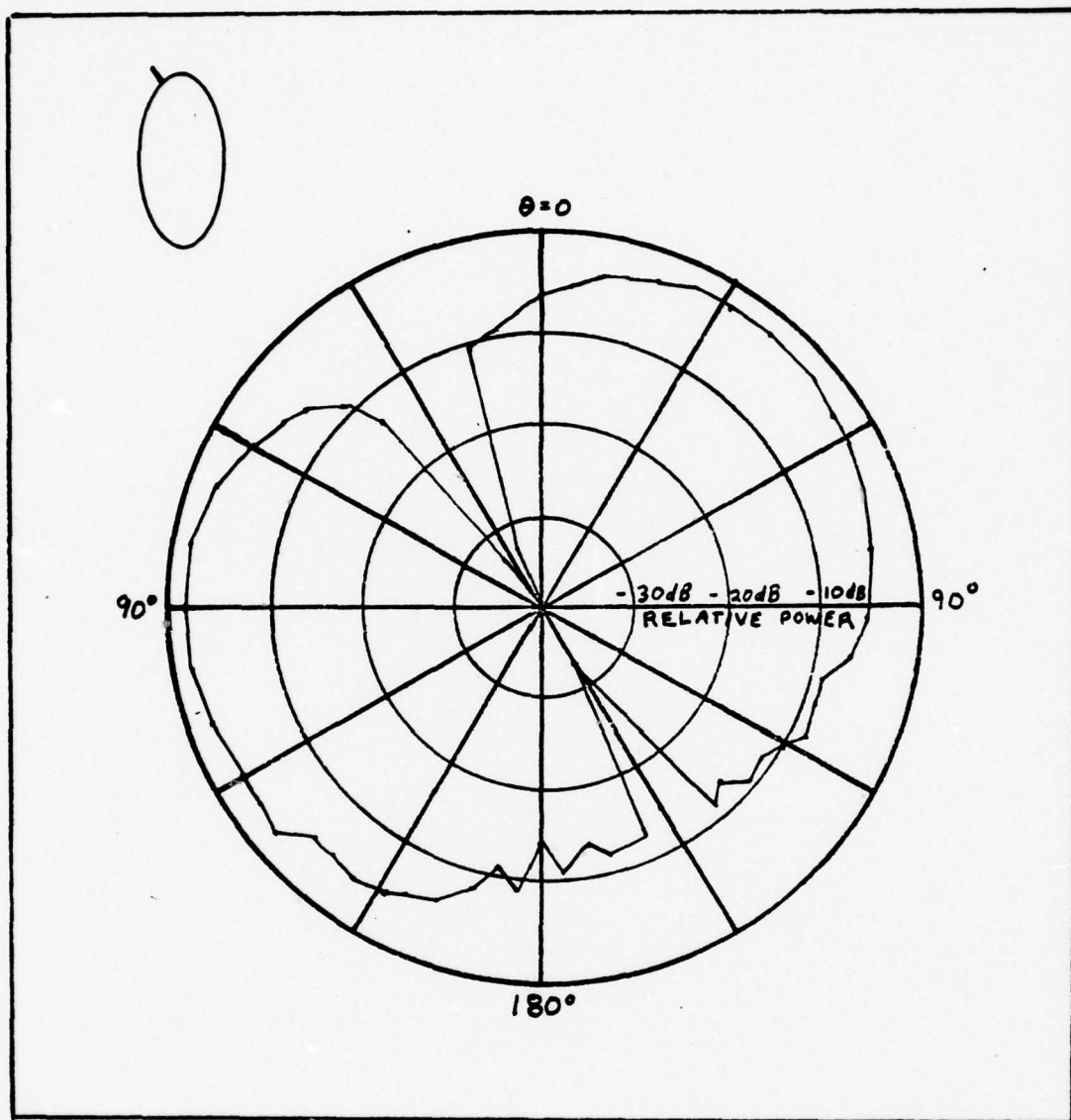
Fig. 13.   Antenna pattern of monopole mounted at
$\Theta = 14^{\circ}$ on a 2λ by 4λ elliptical cylinder.
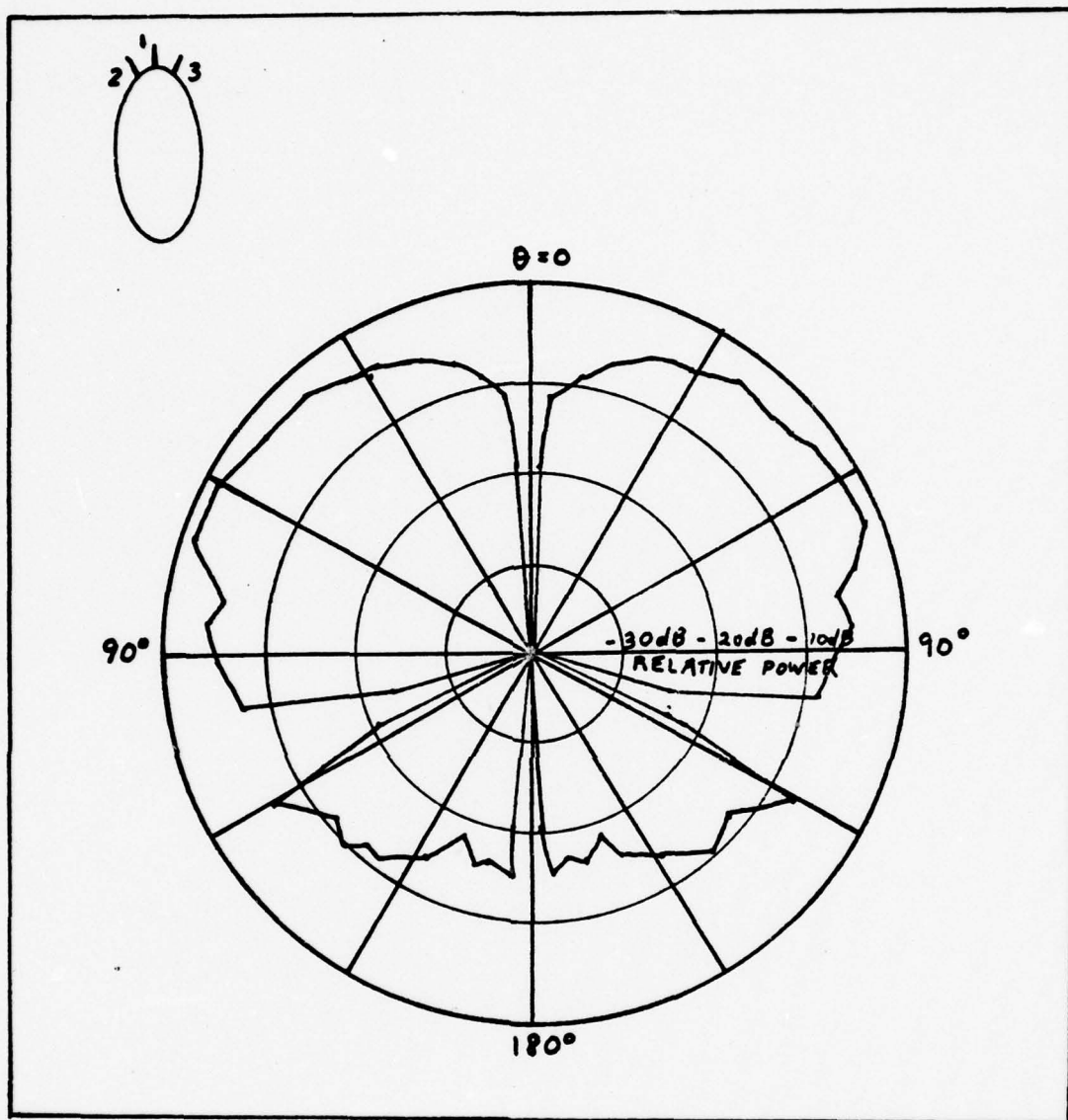
Fig. 14.   Antenna pattern of array in Fig. 1 with
all elements driven in phase
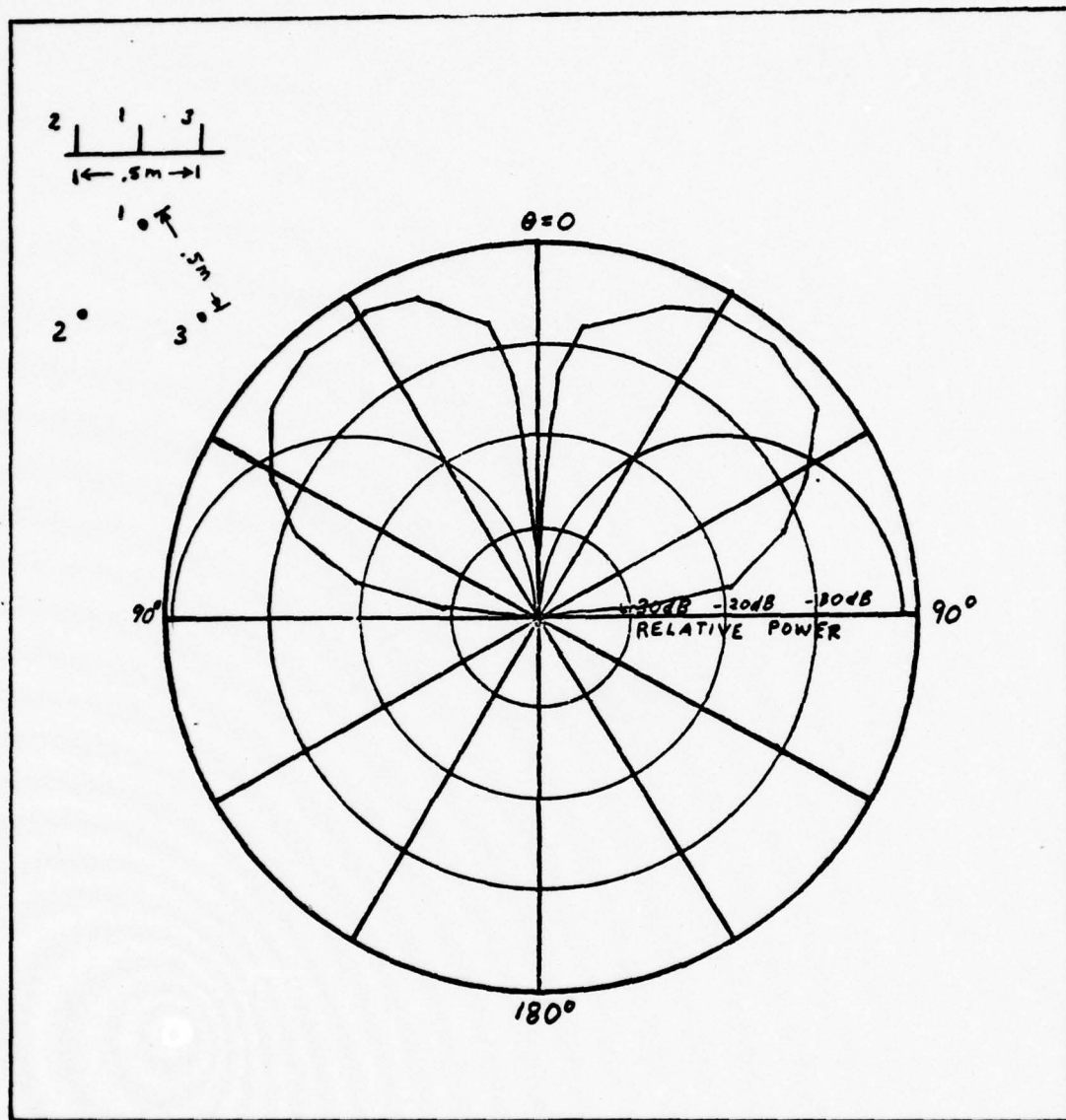
Fig. 15. Antenna pattern of 3 element array on an infinite ground plane, all elements driven in phase.
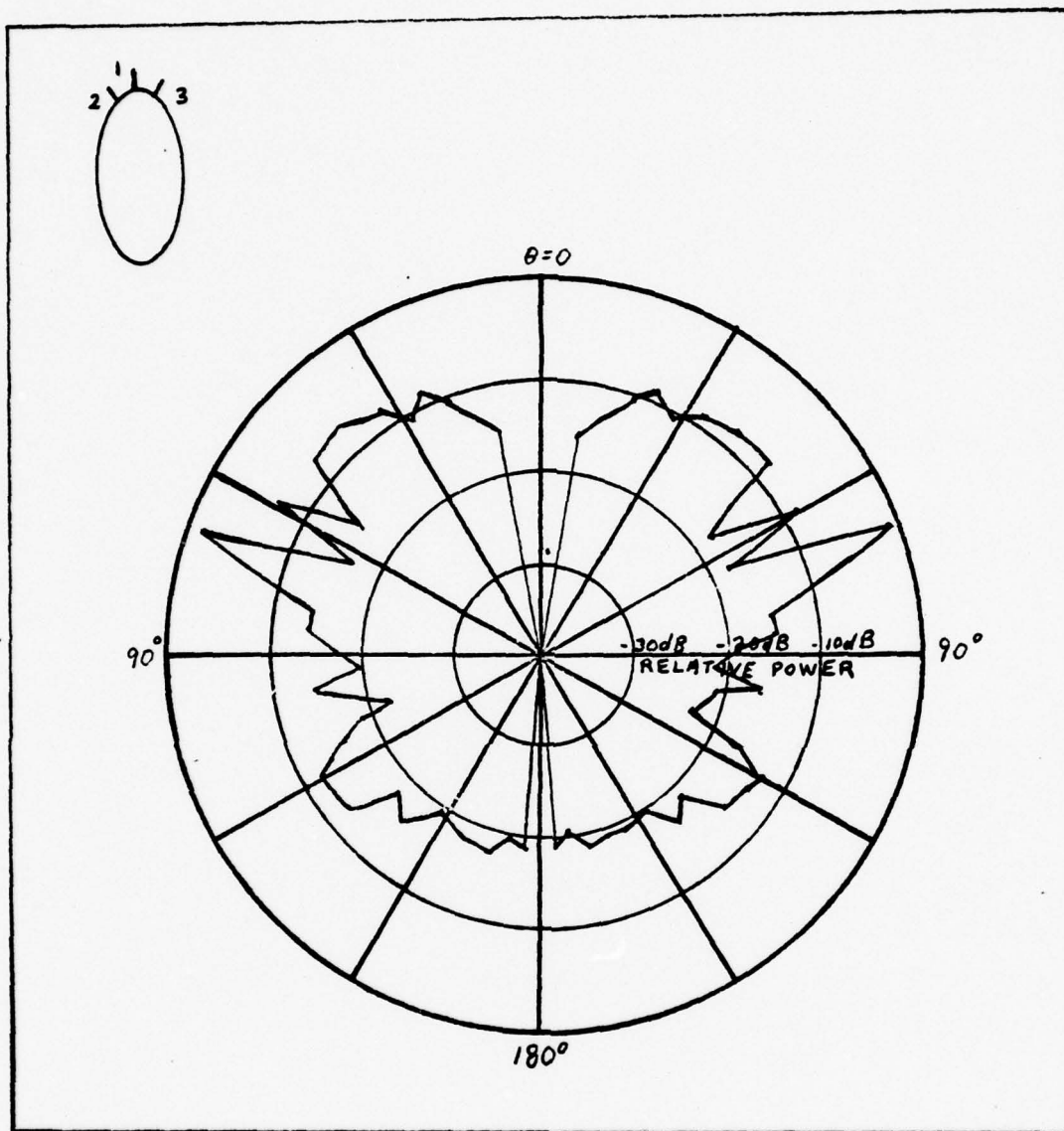
Fig. 16. Antenna pattern of array in Fig. 1
with element 1 driven 45° out of
phase with elements 2 and 3.

V. Conclusions

The geometrical theory of diffraction has been extended to treat monopoles on perfectly conducting cylinders of variable curvature. Following Pathak's approach (Ref 23:19-20) of defining a launch coefficient for a slot in a cylinder, a launch coefficient for a monopole was obtained. For the monopole case, the launch coefficients are the same as for an axially mounted and a length wise mounted slot superimposed on each other.

By carefully keeping track of the distance traveled by the diffracted rays an interference pattern for two or more rays or two or more sources was obtained. If the field pattern is analyzed in such a way as to let the observation distance approach infinity, then the phase could be approximated as the phase at the diffraction point for the ray leaving the cylinder (Q_2). In the illuminated region the phase would be assumed to be that of the source. Although this approximation is valid it was assumed for this problem that since this antenna is to serve as an air to air communications link that the range was not infinite. A nominal distance between communication points of 300 meters was assumed such as to account for aircraft in close proximity to each other. The field further out will just have a smaller ripple on the lobe boundary due to the phases of the wavefronts being nearer the same as a function of their distance allowing the previous approximation to be valid.

The effect of the cylinder is to broaden the beamwidth in the principle plane. By mounting the antenna perpendicular to the surface, the condition of the antennas not being parallel in the x, y

38

plane resulted. Linear array theory was therefore not valid (i.e., an array factor is not present). If the antenna were mounted parallel to each other, the effect would be similar (in the lit region) to tilting a monopole on a flat ground plane so that one side of the beam is directed into instead of along the ground plane. Again, linear antenna theory would not apply. If the field point is in the deep shadow region of all three elements of the array then the result is an equivalent linear array summation at the diffraction point Q_2 but it is only valid for that field point producing a tangent at Q_2. It can also be assumed that the angle with which the antenna is attached to the surface and not its angle with respect to the center of the cylinder controls the location of the nulls.

The array analyzed provides a broad beam for communication problems but with high mobility of nulls for a null steering use. Due to the creeping wave effect, it appears it would be very hard to create a single beam in one general direction. The symmetrical cylinder would tend to cause multiple lobes as in Fig. 16. An end fire or broadside pattern in the x, y plane is not readily obtainable because the elements are not parallel. However when analyzing the fields in the x, z plane ($\alpha_s = 0$, 180) the antenna elements appear to be a linear array with antenna 2 and 3 reduced in height. Planes of view in between ($0 < \alpha_s < 90$) would be a combination of the two approachs although the GTD can still be applied directly and obtain valid results.

Bibliography

1. Carter, P. S., "Antenna Arrays Around Cylinders," Proceedings of the IRE, 31:671-693 (December 1943).

2. Carter, P. S., "Antenna and Cylindrical Fuselage," Report No. 895-11, Rocky Point, RCA Laboratories, N.Y. (December 24, 1943).

3. Sinclair, G., "The Patterns of Antennas Located Near Cylinders of Elliptical Cross Section," Proceedings of the IRE, 39:660-668 (June 1952).

4. Richmond, J. H., "A Wire-Grid Model for Scattering by Conducting Bodies," IEEE Transactions on Antennas and Propagation, AP-14:782-786 (November 1966).

5. Richmond, J. R., "Computer Analysis of Three-Dimensional Wire Antennas," Report 2703-4, The Ohio State University Electroscience Laboratory, Department of Electrical Engineering; prepared under Contract DAAD 05-69-C-0031 for Ballistic Research Laboratory (22 December 1969).

6. Wang, N. M., "Sinusoidal Reaction Formulation for Radiation and Scattering from Conducting Surfaces," IEEE Transactions on Antennas and Propagation, AP-23:376-382 (May 1975).

7. Balanis, C. A., "Aperture Radiation from an Axially Slotted Circular Conducting Cylinder using Geometrical Diffraction Theory," IEEE Trans. Antennas and Propagation, AP-17:507-513 (July 1969).

8. Balanis, C. A., and Peters, L., "Analysis of Aperature Radiation from an Axially Slotted Circular Conducting Cylinder Using Geometrical Theory of Diffraction," IEEE Trans. Antennas and Propagation, AP-17:93-97 (January 1969).

9. Balanis, C. A., "Radiation from TE_{10} Mode Slots on Circular and Elliptical Cylinders," IEEE Trans. Antennas and Propagation, AP-18:400-403 (May 1970).

10. Ryan, C. E., Jr., "Analysis of Radiation Patterns of Antennas on Finite Circular Cylinders and Conically-Capped Cylinders," Report 2805-2, the Ohio State Electroscience Laboratory, Dept. of Electrical Engineering. Prepared under contract DAA21-69-C-0533 for Picatinny Arsenal.

11. Burnside, W. D., Gilreath, M. C., Marhefka, R. J. and Yu, C. L., "A Study of KC-135 Aircraft Antenna Patterns," IEEE Trans. on Antennas and Propagation, AP-23:309-316 (May 1975)

12. Burnside, W. D., "Analysis of On-Aircraft Antenna Patterns," Report 3390-1, the Ohio State University Electroscience Laboratory, Department of Electrical Engineering, prepared under contract N62269-72-C-0354 for Naval Air Developement Center (August 1972). (AD 777 989)

13. Marhefka, R. J., and Burnside, W. D., "Numerical Solutions to some On-Aircraft Antenna Pattern Problems," Technical Report 3390-4, the Ohio State University Electroscience Laboratory, Department of Electrical Engineering. Prepared under contract N62269-72-C-0354 for Naval Air Developement Center (October 1973).

14. Yu, Chong L., "Volumetric Pattern Analysis of Fuselage Mounted Airborne Antennas," Ph.D. Dissertation, Columbus, Ohio (April 1976) NTIS Library no. N76-22419.

15. Levy, B. R., ane Keller, J. B., "Diffraction by a Smooth Object" Communications in Pure and Applied Mathematics, 12;159-209 (February 1959).

16. Franz, W., and Depperman, K., "Theorie der Beugang Am Zylinder unter Berucksichtigung der Kreisshivelle," Ann of Physik,10; 361-373 (June 1952).

17. Franz, W., and Depperman, K., "Theorie der Beugang Am Zylinder unter Berucksichtigung der Kreischwelle," Ann. of Physik, 14; 253-264 (June 1954).

18. Kouyoumjian, R. G., "Asymptotic High-Frequency Methods," Proceedings of the IEEE,53;864-876 (August 1965).

19. Weeks, W. L., Antenna Engineering. New York: McGraw-Hill Book Co., 1968).

20. Voltmer, D. R., "Diffraction by Doubly Curved Convex Surfaces," Ph.D. Dissertation, The Ohio State University (1970)

21. Logan, Nelson A., "General Research in Diffraction Theory," Vol. 2, Report LMSD-288088, Missles and Space Division, Lockheed Aircraft Corporation, (December 1972). (AD241 228, AD243 182)

22. Pathak, P. H., and Luebbers, R. J., "An Analysis of the Radiation from Monopoles in Curved Surfaces," Report in preparation for publication, The Ohio State University Electroscience Laboratory, Department of Electrical Engineering.

' 23. Pathak, P. H., and Kouyoumjian, R. G., "The Radiation from Apertures in Curved Surfaces," NASA, Washington, D.C., Report NASA CR-2263. Prepaired under grant NGR 36-008-144 to the Electroscience Laboratory, Department of Electrical Engineering Ohio State University, Columbus (July 1973).

24. Harrington, R. R., *Time Harmonic Electromagnetic Fields*, New York: McGraw-Hill Book Co., 1961.

25. Bowman, J. J., Senior, and Uslenghi, P. L. E. (Ed's) *Electromagnetic and Acoustic Scattering by Simple Shapes*. North Holland Publishing Co., 1969, pp. 380-395.

26. Tyras, G., *Radiation and Propagation of Electromagnetic Waves*, New York and London, Academic Press, 1969.

Appendix A

Derivation of D_m and α_m

The first step is to formulate and solve the boundary value problem of diffraction of a cylindrical wave by a circular cylinder of radius a. Then the solution will be expanded asymptotically for large values of ka.

In order to simplify computations and avoid repetition, a scalar field is assumed with conditions stated to allow for hard and soft boundary conditions. This scalar field $u(r,\Theta)$ must satisfy the equation

$$(\nabla^2 + k^2)u = \delta(r - \rho)\delta(\Theta) \tag{54}$$

Two different boundary conditions at r = a will be considered. They correspond to different physical problems.

By expanding the diffracted field in cylindrical wave functions and imposing the boundary conditions (Ref 24:Ch. 5) the field for the ray OQ_1Q_2P as shown in Fig. 17 becomes

$$u = \frac{-j}{4}\sum_{m=-\infty}^{\infty}\exp(-jm\Theta)\left[J_m(kr_<) - \frac{GJ_m(ka)}{GH_m^{(2)}(ka)}H_m^{(2)}(kr_<)\right]H_m^{(2)}(kr_>) \tag{55}$$
$$r > a$$

Here $r_>$ and $r_<$ are, respectively, the larger and smaller of the quantities r and ρ.

43
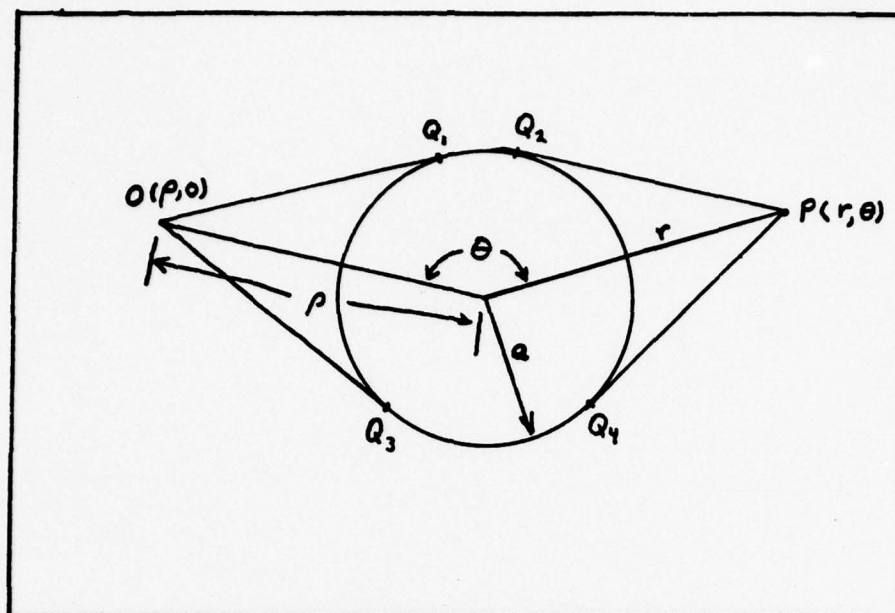
Fig. 17. Geometry for Diffraction

The operator G, which is determined by the boundary conditions as given in Table II.

Table II

The Operator G

	G	Boundary condition		Field Equivalent
Case I:	1	$u = 0$	s	$u = E_z$; perfectly conducting cylinder
Case II:	$\frac{\partial u}{\partial n}$	$\frac{\partial u}{\partial n} = 0$	h	$u = H_z$; perfectly conducting cylinder

The representation of the field as given by Eq. (55) is valid only for small values of ka. A numerically useful result for large values of ka is obtained by employing the well-known Watson transformation which leads to an asymptotic expansion of the field.

44

Accessible descriptions of the method are given in References 25 and 26.

Letting C be a contour encircling the real axis as shown in Fig. 18, the sum in Eq. (55) becomes

$$u = -\frac{1}{8}\int_C \frac{\exp(j\nu(\theta - \pi))}{\sin(\nu\pi)} \frac{H_\nu^{(2)}(kr_>)}{GH_\nu^{(2)}(ka)}$$

$$\cdot (GH_\nu^{(2)}(ka)J_\nu(kr_<) - GJ_\nu(ka)H_\nu^{(2)}(kr_<))d\nu \qquad (56)$$

When ν is replaced by $-\nu$ on that part of the contour for which $\mathcal{I}_m < 0$, Eq. (56) becomes

$$u = -\frac{1}{4}\int_D \frac{\cos(\nu(\theta - \pi))}{\sin(\nu\pi)} \frac{H_\nu^{(2)}(kr_>)}{GH_\nu^{(2)}(ka)}$$

$$\cdot (GH_\nu^{(2)}(ka)J_\nu(kr_<) - GJ_\nu(ka)H_\nu^{(2)}(kr_<))d\nu \qquad (57)$$
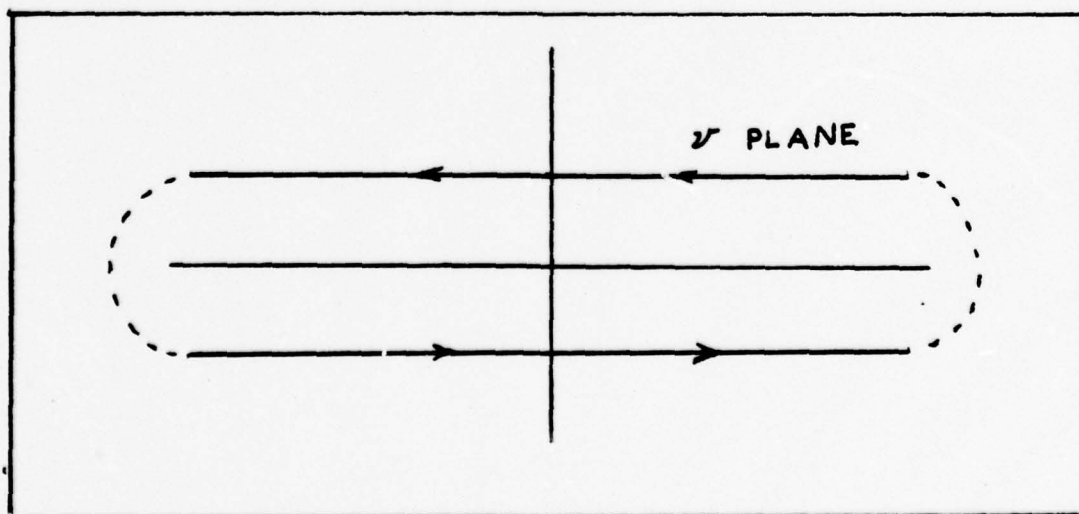
Fig. 18. The path of integration for the Watson type integral representation of the field diffracted by cylinder

45

If the point (r, Θ) lies in the geometrical shadow, the contour D can be closed in the lower half-plane. The integral can now be evaluated by computing the residues at the zeroes ν_m of $GH_\nu^{(2)}(ka)=0$. This yields

$$u = -\frac{\pi j}{4} \sum_{m=1}^{\infty} \frac{\cos(\nu_m(\Theta - \pi))}{\sin(\nu_m \pi)} \frac{GH_{\nu_m}^{(1)}(ka)}{\frac{\partial}{\partial \nu}GH_{\nu_m}^{(2)}(ka)} H_{\nu_m}^{(2)}(kr) H_{\nu_m}^{(2)}(k\rho) \quad (58)$$

The values for ν_m are given in Table IV, Appendix D. Asymptotically expanding the Hankel function appearing in Eq. (58) (Ref 18:365-866):

$$u \sim \frac{j \exp(-jk((r^2 - a^2)^{1/2} + (\rho^2 - a^2)^{1/2}))}{2k(r^2 - a^2)^{1/4}(\rho^2 - a^2)^{1/4}}$$

$$\cdot \sum_{m=1}^{\infty} \frac{\cos(\nu_m(\Theta - \pi))}{\sin(\nu_m \pi)}$$

$$\cdot \exp(j\nu_m(\cos^{-1}(\tfrac{a}{r}) + \cos^{-1}(\tfrac{a}{\rho}))) \frac{GH_{\nu_m}^{(1)}(ka)}{\frac{\partial}{\partial \nu}GH_{\nu_m}^{(2)}(ka)} \quad (59)$$

Using Euler's equation to replace $-\dfrac{\cos(\nu_m(\Theta - \pi))}{\sin(\nu_m \Theta)}$ yields

$$u \sim \frac{j \exp(-jk((r^2 - a^2)^{1/2} + (\rho^2 - a^2)^{1/2}))}{2k(r^2 - a^2)^{1/4}(\rho^2 - a^2)^{1/4}}$$

$$\cdot \sum_{m=1}^{\infty} \frac{\exp(-j\nu_m \Psi_1) + \exp(-j\nu_m \Psi_2)}{1 - \exp(-j2\pi\nu_m)}$$

$$\cdot \exp(j\nu_m(\cos^{-1}(\tfrac{a}{r}) + \cos^{-1}(\tfrac{a}{\rho}))) \frac{GH_{\nu_m}^{(1)}(ka)}{\frac{\partial}{\partial \nu}GH_{\nu_m}^{(2)}(ka)} \quad (60)$$

46

where $\psi_1 = \theta$ and $\psi_2 = 2\pi - \theta$. Eq. (60) contains the leading terms in the asymptotic expansion of the field in the shadow region.

To calculate the GTD field, Eq. (12) in the text of the thesis is used as a starting point. For a torsionless* surface path on a cylinder, no E field exists in the $\hat{b}$ direction so Eq. (10) is equal to zero and Eq.(12) may be written as

$$u = u_i \sqrt{\frac{d\eta_1}{d\eta_2}} \sqrt{\frac{\rho}{s(\rho + s)}} \exp(-jk(\ell + s)$$

$$\cdot \sum_{m=1}^{\infty} D_m(Q_1) D_m(Q_2) \exp\left[-\int_{Q_1}^{Q_2} \alpha_m(\ell) d\ell\right] \tag{61}$$

with

$$u_i = \frac{-jI\omega\mu}{\sqrt{8kR}} \exp(-j(kR + \varphi)) \tag{62}$$

Due to the symmetry of the problem it is clear that the geodesics are arcs of the generating circle of the cylinder. Furthermore, the quantity $d\eta_1/d\eta_2$ has the value unity since a band of diffracted rays does not spread on the cylinder. Also, the radius of curvature ρ in Eq. (61) is infinite so that $(\rho/(\rho + s)s)^{1/2}$ assumes its limiting value $s^{-1/2}$. Moreover, because the geodesic curvature of a ray is constant, the quantities $\alpha_m(\ell)$ and $D_m(\cdot)$ are constants with $D_m(Q_1) = D_m(Q_2)$. Introducing these simplifications into Eq.(61) and using Eq. (62), noting that R at Q_1 is $(\rho^2 - a^2)^{1/2}$. Then Eq. (61) becomes

---

*A torsionless surface path is one where the direction of $\hat{b}$ does not change along a geodesic path on the cylinder.

47

$$u = \frac{-jI\omega\mu}{\sqrt{8ks}(\rho^2 - a^2)^{1/2}}\exp(-j(k((\rho^2 - a^2)^{1/2} + s) + \varphi))$$

$$\cdot \sum_{m=1}^{\infty}D_m^2(Q)\exp(-jk - \alpha_m)\ell) \tag{63}$$

Eq. (63) gives the field associated with any ray from O to P having an arc length ℓ on the cylinder. For the ray OQ_1Q_2P, the length ℓ for a circle has the value $\ell_0 = a\theta - a\cos^{-1}(a/\rho) - a\cos^{-1}(a/r)$, while $s = (r^2 - a^2)^{1/2}$. In addition to this ray, all of the rays which are tangent to the cylinder at Q_1 and encircle the cylinder g times before emerging at Q_2 are also diffracted rays through P. For these rays ℓ has the value $\ell_g = \ell_0 + 2g\pi a$. Inserting this value of ℓ into Eq. (63) and summing over g, the diffracted field at P due to those rays which are tangent at Q_1 is given by

$$u = \frac{-jI\omega\mu}{\sqrt{8k}(\rho^2 - a^2)^{1/4}(r^2 - a^2)^{1/4}}\exp\left[-j(k((\rho^2 - a^2)^{1/2} + (r^2 - a^2)^{1/2})+\varphi)\right]$$

$$\cdot \sum_{m=1}^{\infty}D_m^2\exp((-jk - \alpha_m)\ell_0)(1 - \exp(2\pi(-jka - a\alpha_m)))^{-1} \tag{64}$$

Along with the family of rays described above, there exists other rays which are tangent to the cylinder at Q_3, encircle the cylinder g times and then emerge tangentially at Q_4 and pass through P. Computing the field along these rays yields a result of the form of Eq. (64) with θ replaced by $2\pi - \theta$ in ℓ_0. Adding this result to Eq. (65), we obtain for the total diffracted field at P

$$u = \frac{-jI\omega\mu\exp(-jk((\rho^2 - a^2)^{1/2} + (r^2 - a^2)^{1/2}) + \varphi)}{\sqrt{8k}(\rho^2 - a^2)^{1/4}(r^2 - a^2)^{1/4}}$$

$$\cdot \sum_{m=1}^{\infty} \frac{D_m^2 \exp((-jka - a\alpha_m)\Psi_1) + \exp((-jka - a\alpha_m)\Psi_2)}{1 - \exp(2\pi(-jka - a\alpha_m))}$$

$$\cdot \exp((jka + a\alpha_m)(\cos^{-1}(\tfrac{a}{r}) + \cos^{-1}(\tfrac{a}{\rho}))) \qquad (65)$$

where $\Psi_1 = \theta$ and $\Psi_2 = 2\pi - \theta$. Comparing Eq. (65) to Eq. (60) and ignoring the amplitude and the phase of the source gives

$$\alpha_m = -jk + j\nu_m a^{-1}$$

$$D_m^2 = -\left(\frac{jk}{2\pi}\right)^{-1/2} \frac{GH_{\nu_m}^{(1)}(ka)}{\frac{\partial}{\partial\nu}GH_{\nu_m}^{(2)}(ka)} \qquad (66)$$

Expansion of $GH_{\nu_m}^{(1)}(ka)/\left[(\partial/\partial\nu)GH_{\nu_m}^{(2)}(ka)\right]$ is done in Appendix D.

Voltmer's generalizations for surfaces of variable curvature are contained in Table I in the text, and are seen to be dependent on not only ρ_g, the radius of curvature of the surface with respect to arc length along the ray trajectory, but also $\dot{\rho}_g$, $\ddot{\rho}_g$, and ρ_{tn}, where the dot denotes a derivative with respect to arc length and ρ_{tn} is the radius of curvature of the surface in the direction of the binormal to the ray.

Appendix B

The Launching Coefficient

The launching coefficinet is derived by asymptotically expanding a canonical problem for ka large and comparing this to the GTD solution as was done for the diffraction coefficients in Appendix A. Start with Eq. (58) in Appendix A.

$$u = -\frac{j\pi}{4}\sum_{m=1}^{\infty} \frac{\cos(\nu_m(\theta - \pi))}{\sin(\nu_m\pi)} \frac{GH_{\nu_m}^{(1)}(ka)}{\frac{\partial}{\partial\nu}GH_{\nu_m}^{(2)}(ka)} H_{\nu_m}^{(2)}(kr)H_{\nu_m}^{(2)}(k\rho) \tag{58}$$

Replacing $\dfrac{\cos(\nu_m(\theta - \pi))}{\sin(\nu_m\pi)} = \dfrac{\exp(-j\nu_m\Psi_1) + \exp(-j\nu_m\Psi_2)}{1 - \exp(-j2\pi\nu_m)}$, and letting

$(1 - \exp(-j2\pi\nu_m))^{-1} = 1$ for ka large gives

$$u = -\frac{j\pi}{4}\sum_{m=1}^{\infty} \frac{GH_{\nu_m}^{(1)}(ka)}{\frac{\partial}{\partial\nu}GH_{\nu_m}^{(2)}(ka)} H_{\nu_m}^{(2)}(ka)H_{\nu_m}^{(2)}(k\rho)$$

$$\cdot \quad \exp(-j\nu_m\Psi_1) + \exp(-j\nu_m\Psi_2) \tag{67}$$

where $\Psi_1 = \theta$ and $\Psi_2 = 2\pi - \theta$. Using the definition of the diffraction coefficient from Appendix A

$$\frac{GH_{\nu_m}^{(1)}(ka)}{\frac{\partial}{\partial\nu}GH_{\nu_m}^{(2)}(ka)} = -\left(\frac{jk}{2\pi}\right)^{1/2}D_m^2 \tag{66}$$

and the asymptotic expansion

50

$$H_{\nu}^{(2)}(k\rho) \sim \sqrt{\frac{2}{\pi k \rho}} \exp(k_{\rho} - (2\nu + 1)\frac{\pi}{4}) \tag{68}$$

and defining the boundary conditions as

$$\frac{\partial}{\partial n'} u(\bar{\rho}', \bar{\rho}) = 0 \text{ for } \rho' = a \quad \text{(hard boundary)} \tag{69}$$

and

$$u(a\hat{\rho}', \bar{\rho}) = 0 \quad \text{(soft boundary)} \tag{70}$$

then for the hard boundary condition, noting the results for a point source in Eq. (23)

$$E_{\theta}(\bar{\rho}) = I_x \frac{\partial}{\partial \rho} u(\bar{\rho}, \hat{x}a) \tag{71}$$

Then Eq. (67) becomes

$$E_{\theta} = -\frac{jkI_x}{\sqrt{8\pi kj}} \sum_{m=1}^{\infty} \left[-j\pi(\frac{jk}{2})^{1/2} H_{\nu_m}^{(2)}(ka)D_m^h \right]$$

$$\cdot \left[\exp(-j\nu_m \Psi_1) + \exp(-j\nu_m \Psi_2) \right]$$

$$\cdot D_m^h \frac{\exp(-jk\rho)}{\sqrt{\rho}} \tag{72}$$

Referring to Fig. 17, the GTD solution for E with a launching coefficient replacing the field incident at Q_1 is

$$E_{\theta} = CI_x \sum_{m=1}^{\infty} L_m^h D_m^h \left[\exp((-jka - a\alpha_m^h)\Psi_1) \right.$$

$$\left. + \exp((-jka - a\alpha_m^h)\Psi_2) \right] \frac{\exp(-jk\rho)}{\sqrt{\rho}} \tag{73}$$

51

Comparing Eqs. (72) and (73) gives

$$C = -\frac{k^- \exp(j\pi/4)}{\sqrt{8\pi k}} \tag{74}$$

$$L_m^h = -j\pi\left(\frac{jk}{2\pi}\right)^{1/2} H_{\nu_m}^{(2)}(ka) D_m^h \tag{75}$$

$$\alpha_m^h = ka - j\alpha_m^h a \tag{75}$$

Replacing the hard coefficients with the soft coefficients and
differentiating $H_{\nu_m}^{(2)}(ka)$ with respect to ka will solve the problem
for the soft boundary condition. $H_{\nu_m}^{(2)}(ka)$ and $H_{\nu_m}^{(2)'}(ka)$ are ex-
panded in Appendix D.

Comparing this to Pathak's work on slots in cylinders (Ref 23:
46-62) shows that the same launch coefficient results for a magnetic
current source in the $\hat{z}$ direction. The soft boundary condition for
a monopole is equivalent to a launch coefficient of a magnetic line
source oriented in the $\hat{\theta}$ direction (circumferential slot). The
monopole can then be modeled as 2 magnetic line sources perpendicular
to the direction of the monopole electric source for fields in the
deep shadow region.

Appendix C

Airy Functions, Derivatives and Zeros⁻

The Airy differential equation,

$$\frac{d^2 w(z)}{dz^2} - zw(z) = 0 \tag{76}$$

yields two independent solutions which assumes several forms. The form used in this thesis is defined by Miller as

$$Ai(z) = \frac{1}{2\pi j} \int_{\Gamma_1} \exp(zt - t^3/3) dt \tag{77}$$

which for $z = x$ (x real) may be written as

$$Ai(x) = \frac{1}{\pi} \int_0^\infty \cos(xt + t^3/3) dt \tag{78}$$

Γ_1 is shown in Figure 19. A second independent solution is given by

$$Ai(ze^{-j2\pi/3}) = \frac{1}{2\pi j} \int_{\Gamma_1} \exp(ze^{-j2\pi/3} t - t^3/3) dt$$

$$= \frac{e^{j2\pi/3}}{2\pi j} \int_{\Gamma_2} \exp(zt - t^3/3) dt \tag{79}$$

while the Wronskian relation satisfied by these solutions is
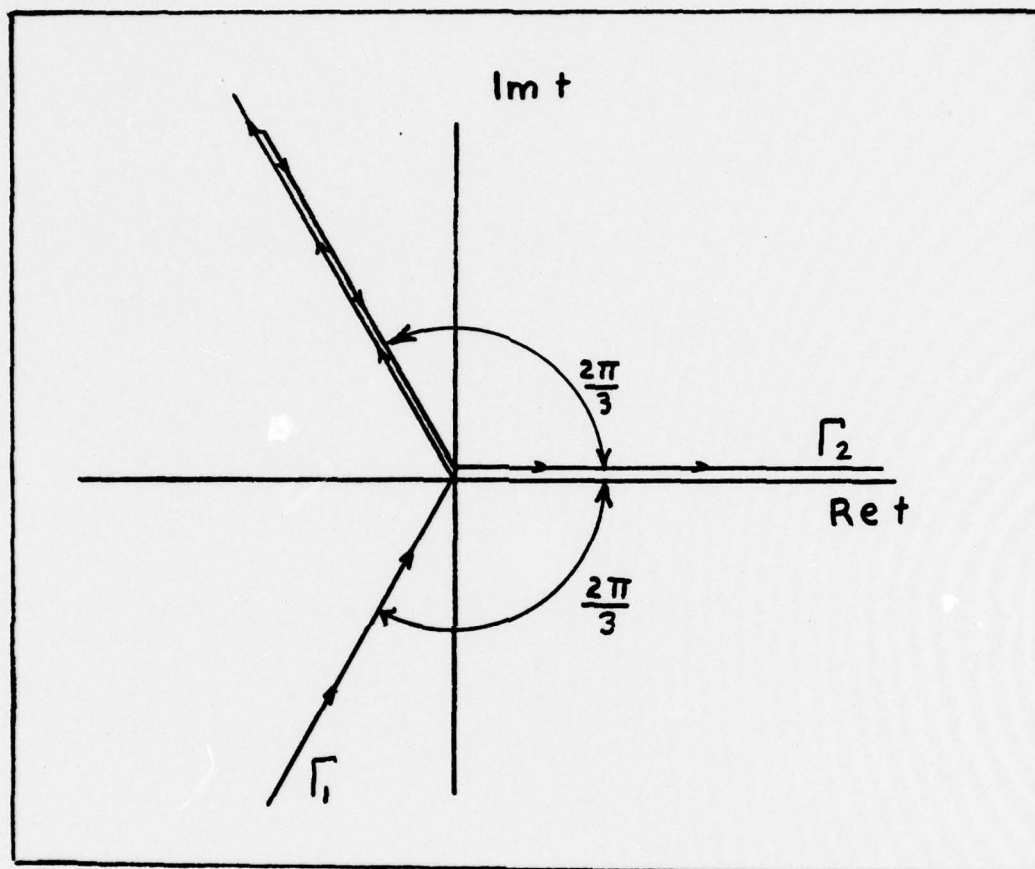
Fig. 19. Airy Function contours of integration

$$\frac{e^{j\pi/6}}{2\pi} = Ai(z)Ai'(ze^{-j2\pi/3})e^{-j2\pi/3} - Ai(ze^{-j2\pi/3})Ai'(z) \qquad (80)$$

The derivatives are obtained by differentiating under the integrals of Eqs. (77) and (79).

The roots of the Airy function and its derivative which satisfy

$$Ai(z) = 0 \qquad\qquad and \qquad\qquad Ai'(z) = 0$$

are real and negative and are denoted as $-q_m$ and $-\bar{q}_m$, respectively, where m denotes the number of the root. The first two roots are presented in Table III as are the values of $Ai(-\bar{q}_m)$ and $Ai'(-q_m)$.

Table III

Airy Functions, Derivatives, and Zeros

m	q_m	$\bar{q}_m$	$Ai'(-q_m)$	$Ai(-\bar{q}_m)$
1	+2.33811	+1.01879	+0.70121	+0.53566
2	+4.08795	+3.24820	-0.80311	-0.41902

(from Ref 20:149)

Appendix D

Hankel Functions

An evaluation of the integral resulting from the Watson transformation requires the calculation of the roots of the equation

$$GH_{\nu}^{(2)}(ka) = 0 \qquad (81)$$

where

$$G = \begin{cases} 1 & \text{Soft EM cylinder} \\ \\ \dfrac{\partial}{\partial x}\Big|_{x=ka} & \text{Hard EM cylinder} \end{cases}$$

A closed-form evaluation of these zeros is not possible. However, an asymptotic representation of the roots may be obtained for large values of ka. The procedure is outlined in Reference 20, pages 127 to 133. The results are listed in Tables IV and V on the next page. The asymptotic approximations for the Hankel functions of the second order are

$$H_{\nu_m}^{(2)}(ka) \sim 2\, e^{j\frac{\pi}{3}}\left(\frac{2}{ka}\right)^{1/3} Ai(-\bar{q}_m)\left\{1 + \left(\frac{2}{ka}\right)^{2/3} e^{j\frac{2\pi}{3}}\right\} \qquad (82)$$

$$H_{\nu_m}^{(2)}{}'(ka) \sim -2e^{-j\frac{\pi}{3}}\left(\frac{2}{ka}\right)^{2/3} Ai'(-q_m)\left\{1 - \left(\frac{2}{ka}\right)^{2/3}\frac{q_m}{15}e^{j\frac{2\pi}{3}}\right\} \qquad (83)$$

an alternative form is

$$H_{\nu}^{(2)}(k\rho) \sim \sqrt{\frac{2}{\pi k\rho}}\exp -j(k\rho - (2\nu + 1)\frac{\pi}{4}) \qquad (68)$$

56

Table IV

Hankel Function Zeros, $GH_{\nu}^{(2)}(ka) = 0$

Surface	Zeros-ν
Soft	$\nu_m = ka + q_m e^{-j\pi/3}\left(\frac{ka}{2}\right)^{1/3} - \frac{q_m^2}{60}e^{j\pi/3}\left(\frac{ka}{2}\right)^{-1/3}$
Hard Cylinder	$\bar{\nu}_m = ka + \bar{q}_m e^{-j\pi/3}\left(\frac{ka}{2}\right)^{1/3} - \frac{\bar{q}_m^2}{60}\left(1+\frac{6}{\bar{q}_m^3}\right)\left(\frac{ka}{2}\right)^{-1/3}$

(from Ref 20;145)

Table V

Hankel Function Quotient, $\dfrac{GH_{\nu}^{(1)}(ka)}{\frac{\partial}{\partial\nu}GH_{\nu}^{(2)}(ka)}$

Surface	G-Operator	Quotient
Soft	1	$\dfrac{e^{-j5\pi/6}\frac{ka}{2}^{1/3}}{2\pi(Ai'(-q_m))^2}\left(1 + \left(\frac{2}{ka}\right)^{2/3}\frac{q_m}{30}e^{-j\pi/3}\right)$
Hard	$\dfrac{\partial}{\partial(ka)}$	$\dfrac{e^{-j5\pi/6}\left(\frac{ka}{2}\right)^{1/3}}{2\pi\bar{q}_m(Ai(-\bar{q}_m))^2}\left(1 + \left(\frac{2}{ka}\right)^{2/3}\frac{\bar{q}_m}{30}e^{-j\pi/3}\right)$

(from Ref 20:136)

Appendix E

The Field in the Transition Region

The material for this Appendix is taken in part from Reference 23, pages 63 to 70. In the transition region adjacent to the shadow boundary, the representation of the field radiated by the monopole described by the launching coefficient in Appendix B is poorly convergent so a different form is needed. It will be seen that a suitable asymptotic solution can be obtained in terms of integrals. The first order approximation is adequate for $ka > 3$, and since the added complexity is hard to justify, only the first order will approximation will be derived.

For the principle plane analysis of the cylinder (looking length-wise down the cylinder), only the hard boundary condition exists, therefore only it will be treated. The soft condition is solved identically as below except without taking the $\partial u / \partial \rho$.

The Watson transform is again applied to Eq. (55), but this time the resulting expression is left in the form of an integral. In the far zone, $H_\nu^{(2)}(k\rho)$ is approximated asymptotically as in Eq. (68) so that (see Ref 18:865-866)

$$\frac{\partial u}{\partial \rho} \quad \frac{-k}{2\sqrt{8\pi k j}} \frac{\exp(-jk\rho)}{\sqrt{\rho}} \sum_{\ell=0}^{\infty} \int_{-\infty}^{\infty} d\nu$$

$$\cdot \frac{H_\nu^{(1)\prime}(ka)H_\nu^{(2)}(ka) - H_\nu^{(2)\prime}(ka)H_\nu^{(1)}(ka)}{H_\nu^{(2)}(ka)}$$

$$\cdot \quad \exp(-j\nu(\Psi_1 + 2\pi\ell)) + \exp(-j\nu(\Psi_2 + 2\pi\ell)) \quad (84)$$

From the Wronskian relationship for the Hankel function,

$$H_m^{(1)\prime}(ka)H_m^{(2)}(ka) - H_m^{(2)\prime}(ka)H_m^{(1)}(ka) = \frac{4j}{\pi ka} \tag{85}$$

then

$$\frac{\partial u}{\partial \rho} \sim -\frac{2jk \; \exp(-jk\rho)}{ka\sqrt{8\pi kj} \; \sqrt{\rho}} \sum_{\ell=0}^{\infty} \int_{-\infty}^{\infty} dm \;\cdot$$

$$\frac{(\exp(-jm(\psi_1 + 2\pi\ell))) + \exp(-jm(\psi_2 + 2\pi\ell))}{H_m^{(2)}(ka)} \tag{86}$$

Replacing $H_m^{(2)}(ka)$ by its Watson approximations (for $m \sim ka \gg 1$) gives rise to the Fock function representations for the $\partial u/\partial \rho$:

$$\frac{\partial u}{\partial \rho} \sim \frac{2}{\pi ka} \frac{-jk}{\sqrt{8\pi kj}} \sum_{\ell=0}^{\infty} \Bigg[\exp(-jka(\psi_1 + 2\pi\ell)) \left(\frac{ka}{2}\right)^{2/3} \cdot$$

$$(-j\sqrt{\pi}) \int_{\Gamma_1} \frac{\exp(-j\xi_1 \tau)}{w_2(\tau)} d\tau + \exp(-jka(\psi_2 + 2\pi\ell)) \; \cdot$$

$$\left(\frac{ka}{2}\right)^{2/3} (-j\sqrt{\pi}) \int_{\Gamma_1} \frac{\exp(-j\xi_2 \tau)}{w_2(\tau)} d\tau \Bigg] \frac{\exp(-jk\rho)}{\sqrt{\rho}} \tag{87}$$

where $H_m^{(2)}(ka) \sim \frac{j}{\sqrt{\pi}} \left(\frac{2}{ka}\right)^{1/3} w_2(\tau)$, and $\xi_{\genfrac{}{}{0pt}{}{1}{(2)}} = \left(\frac{ka}{2}\right)^{1/3} \psi_{\genfrac{}{}{0pt}{}{1}{(2)}}$

Here $W_2(\tau)$ is the Fock-type Airy function related to the Miller-type Airy function by

$$w_2(\tau) = 2\sqrt{\pi}\exp(-j\pi/6)A_i(-\tau\exp(j\pi/3)) \tag{88}$$

or

$$= \frac{1}{\sqrt{\pi}} \int_{\Gamma_2} \exp(\tau z - z^3/3)dz \tag{89}$$

with the contour of integration shown in Appendix C.

Introducing the Fock functions

$$\widetilde{g}(\xi) = \frac{1}{\sqrt{\pi}} \int_{\Gamma_1} \frac{\exp(-j\xi\tau)}{w_2(\tau)} d\tau \tag{90}$$

then Eq. (87) becomes

$$\frac{\partial u}{\partial \rho} \sim -jC\left(\frac{2}{ka}\right)^{1/3} \widetilde{g}(\xi_1)\exp(-jka\psi_1) + \widetilde{g}(\xi_2) \, \cdot$$

$$\cdot \exp(-jka\psi_2) \frac{\exp(-jk\rho)}{\sqrt{\rho}} \tag{91}$$

Where only the $\ell=0$ term is retained for large ka. Substituting this into Eq. (71), the far-zone electric fields for the line source $\hat{x} I_x$ is

$$E_\Theta \sim C \, I_x \left\{ -j\left(\frac{2}{ka}\right)^{1/3} \right\} \cdot$$

$$\cdot \left(\widehat{g}(\xi_1)\exp(-jka\psi_1) + \widetilde{g}(\xi_2)\exp(-jka\psi_2) \right) \, \cdot$$

$$\cdot \frac{\exp(-jk\rho)}{\sqrt{\rho}} \tag{92}$$

Comparing with Eq. (73) yields

$$v(Q_1,Q_2) = -j\sqrt{\frac{d\eta_1}{d\eta_2}}\left(\frac{2}{ka}\right)^{1/3} \widetilde{g}(\xi_1)\exp(-jka\psi_1)\exp(-jk\ell) \tag{93}$$

Tabulation of $\widehat{g}(\xi)$ is included in Appendix G.

Field Data

The following data consists of the field at P due to each antenna. Values were calculated for field points at a constant distance of 300 meters. The angle v is the angle the field radius vector makes with the verticle—the same as the parametric v used in the mathematical model of the cylinder. The field is calculated for v between 0 and 180° in steps of 5°. Due to symmetry the field due to antenna 2 in the 180° to 360° range is the same as for antenna 3 in the 0 to 180° range with the direction of the field vector turned around (shifted 180° spatially).

To calculate the total fields using these tables, add the source phase of the antenna in question to that in the chart for that antenna, and multiply the x and y quantities by the source amplitude. Now for each field point determined by v, an x,y,phase data point for each antenna is taken from the table. To obtain the total field these three vectors are added vectorially.

Also noted are the equations which were used to calculate the values in the chart. The equations are

Eq. #	Equations used
1	Lit region Eq. (40)
2	Lit side of transition region Eq. (41)
3	Shadow side of transition region Eq. (42)
4	Deep shadow region Eq. (43)

Table VI

Field Data
Antenna 1

v	Eq. #	Magnitude	x	y	Phase$\left[-j(\cdot)\right]$
0	1	0.000	0.000	0.000	0.00
5	1	2.944	−0.258	2.933	2.76
10	1	5.865	−1.024	5.766	11.01
15	1	8.740	−2.276	8.438	24.70
20	1	11.545	−3.957	10.798	43.70
25	1	14.259	−6.062	12.906	67.89
30	1	16.861	−8.479	14.574	97.07
35	1	19.330	−11.147	15.791	131.00
40	1	21.646	−13.986	16.521	169.44
45	1	23.793	−16.903	16.744	212.09
50	2	24.000	−18.463	15.337	258.61
55	2	24.510	−22.623	15.659	306.28
60	2	25.068	−21.781	12.409	344.02
65	2	25.479	−23.166	10.627	28.17
70	2	25.555	−23.907	8.589	76.30
75	2	25.480	−24.654	6.436	127.84
80	2	25.026	−24.674	4.182	182.32
85	2	24.304	−22.965	1.958	239.15
90		23.316	−23.316	0.000	3.06
95	3	22.223	−22.138	−1.937	79.95
100	3	21.082	−20.762	−3.661	156.54
105	3	19.826	−19.150	−5.131	231.73
110	3	18.771	−17.639	−6.420	303.32
115	3	17.618	−15.967	−7.446	8.05
120	3	16.366	−14.173	−8.183	73.22
125	3	15.310	−12.541	−8.781	137.67
130	4	14.466	−11.082	−9.299	195.93
135	4	11.399	−8.060	−8.060	208.36
140	4	11.468	−7.372	−8.785	284.12
145	4	10.830	−6.212	−8.871	344.67
150	4	7.950	−3.975	−6.885	50.41
155	4	9.520	−4.023	−8.628	107.02
160	4	6.316	−2.160	−5.935	128.98
165	4	8.580	−2.221	−8.238	164.79
170	4	3.831	−0.665	−3.773	145.14
175	4	7.829	−0.682	−7.800	164.79
180	4	0.000	0.000	0.000	0.00

Table VII

Field Data
Antenna 2

v	Eq. #	Magnitude	x	y	Phase$\left[-j(\cdot)\right]$
0	1	15.418	0.000	15.418	22.90
5	1	17.970	-1.591	17.899	33.46
10	1	20.382	-3.578	20.066	49.28
15	1	22.635	-5.912	21.849	70.24
20	1	24.712	-8.521	23.196	96.17
25	1	25.595	-10.897	23.159	126.87
30	2	25.222	-12.699	21.792	156.53
35	2	25.220	-14.555	20.596	186.01
40	2	25.546	-16.516	19.489	220.88
45	2	25.606	-18.201	18.012	260.81
50	2	30.279	-19.442	16.135	305.37
55	2	24.678	-20.296	14.038	344.71
60	2	23.830	-20.707	11.792	36.77
65	3	22.866	-20.724	9.664	86.77
70	3	21.723	-20.413	7.430	132.00
75	3	20.575	-19.874	5.325	234.78
80	3	19.410	-19.115	3.371	7.94
85	3	18.229	-18.160	1.589	83.45
90	3	17.083	-17.083	0.000	196.85
95	3	15.960	-15.899	-1.391	274.39
100	4	14.854	-14.628	-2.579	352.03
105	4	10.921	-10.590	-2.827	296.08
110	4	10.639	-9.997	-3.639	18.86
115	4	10.469	-9.483	-4.424	110.64
120	4	9.859	-8.538	-4.930	190.99
125	4	8.484	-6.950	-4.866	272.01
130	4	8.274	-6.338	-5.318	347.50
135	4	6.569	-4.645	-4.645	79.73
140	4	7.771	-4.995	-5.953	144.93
145	4	6.136	-3.519	-5.026	189.05
150	4	3.825	-1.912	-3.313	286.93
155	4	7.305	-3.087	-6.621	315.70
160	4	1.370	-0.469	-1.287	325.07
165	4	7.241	-1.874	-6.994	24.83
170	4	6.601	-1.146	-6.501	59.56
175	4	8.130	-0.709	-8.099	9.34
180	4	5.024	0.000	-5.025	117.38

Table VIII

Field Data
Antenna 3

v	Eq. #	Magnitude	x	y	Phase $[-j(\cdot)]$
0	1	15.418	0.000	−15.418	22.90
5	1	12.745	1.110	−12.697	17.67
10	1	9.973	1.732	−9.821	17.83
15	1	7.124	1.844	−6.881	23.36
20	1	4.440	1.443	−3.966	34.23
25	1	1.285	0.543	−1.165	50.35
30	1	1.658	−0.829	1.436	71.60
35	1	4.587	−2.631	3.758	97.81
40	1	7.478	−4.827	5.712	128.78
45	1	10.308	−7.319	7.260	164.27
50	1	13.056	−10.039	8.349	204.00
55	1	15.700	−12.905	8.943	247.67
60	1	18.220	−15.827	9.027	294.94
65	1	20.596	−18.715	8.600	345.45
70	1	20.810	−21.480	7.678	38.80
75	1	24.846	−24.039	6.283	94.60
80	1	25.670	−25.313	4.300	152.40
85	2	25.797	−25.713	2.082	210.15
90	2	25.842	−25.841	0.000	268.30
95	2	25.972	−25.858	−2.431	327.97
100	2	26.147	−25.719	−4.707	11.99
105	2	25.405	−24.496	−6.734	89.95
110	2	24.700	−23.157	−8.594	150.92
115	2	22.770	−20.577	−9.749	212.65
120	3	21.622	−18.725	−10.811	289.60
125	3	21.618	−17.708	−12.400	302.50
130	3	20.368	−15.603	−13.092	0.72
135	3	19.219	−13.590	−13.590	58.52
140	3	18.288	−11.755	−14.009	108.95
145	3	16.926	−9.708	−13.865	161.14
150	3	15.697	−7.848	−13.594	206.92
155	4	14.397	−6.084	−13.048	273.65
160	4	11.630	−3.978	−10.929	304.16
165	4	11.518	−2.981	−11.126	347.81
170	4	8.274	−1.437	−8.148	329.34
175	4	10.593	−0.923	−10.553	345.40
180	4	3.329	0.000	−3.291	290.14

Appendix G

<u>Table</u> <u>of</u> <u>the</u> <u>Hard</u> <u>Fock</u> <u>Function</u>

The function is defined as

$$g(\xi) = \frac{1}{\sqrt{\pi}} \int \exp(-j\xi t) \frac{1}{w_1'(t)} \, dt$$

Table IX

The Hard Fock Function

ξ	Modulus	Argument
-1.00	1.861	15.460
-0.95	1.847	12.626
-0.90	1.833	10.077
-0.85	1.818	7.801
-0.80	1.802	5.785
-0.75	1.785	4.016
-0.70	1.766	2.482
-0.65	1.747	1.174
-0.60	1.726	0.079
-0.55	1.705	359.187
-0.50	1.682	358.487
-0.45	1.658	357.971
-0.40	1.633	357.627
-0.35	1.607	357.446
-0.30	1.580	357.419
-0.25	1.552	357.536
-0.20	1.523	357.790
-0.15	1.493	358.172
-0.10	1.463	358.672
-0.05	1.431	359.284
0.00	1.399	0.000
0.05	1.367	0.812
0.10	1.334	1.713
0.15	1.300	2.696
0.20	1.266	3.755
0.25	1.232	4.883
0.30	1.197	6.074
0.35	1.163	7.323
0.40	1.128	8.624
0.45	1.093	9.971
0.50	1.059	11.360
0.55	1.025	12.786
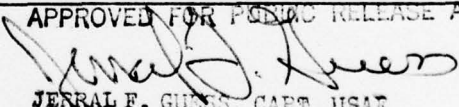
ε	Modulus	Argument
0.60	0.991	14.244
0.65	0.958	15.731
0.70	0.924	17.243
0.75	0.892	18.776
0.80	0.860	20.326
0.85	0.828	21.893
0.90	0.798	23.474
0.95	0.768	25.070
1.00	0.738	26.683

(from Ref 21:ch. 4)

For more accurate values see Ref 21.

REPORT DOCUMENTATION PAGE		READ INSTRUCTIONS BEFORE COMPLETING FORM
1. REPORT NUMBER AFIT/GE/EE/77-41	2. GOVT ACCESSION NO.	3. RECIPIENT'S CATALOG NUMBER
4. TITLE (and Subtitle) ANALYSIS OF MONOPOLE ANTENNA ARRAYS ON CYLINDERS BY THE GEOMETRICAL THEORY OF DIFFRACTION		5. TYPE OF REPORT & PERIOD COVERED MS Thesis
		6. PERFORMING ORG. REPORT NUMBER
7. AUTHOR(s) Bruce A. Thieman		8. CONTRACT OR GRANT NUMBER(s)
9. PERFORMING ORGANIZATION NAME AND ADDRESS Air Force Institute of Technology (AFIT-EN) Wright-Patterson AFB, Ohio 45433		10. PROGRAM ELEMENT, PROJECT, TASK AREA & WORK UNIT NUMBERS
11. CONTROLLING OFFICE NAME AND ADDRESS Mr. Edroas DCID Spread Spectrum Group Rome ADC		12. REPORT DATE December, 1977
		13. NUMBER OF PAGES 74
14. MONITORING AGENCY NAME & ADDRESS(if different from Controlling Office)		15. SECURITY CLASS. (of this report) Unclassified
		15a. DECLASSIFICATION/DOWNGRADING SCHEDULE

16. DISTRIBUTION STATEMENT (of this Report)

Approved for public release; distribution unlimited

17. DISTRIBUTION STATEMENT (of the abstract entered in Block 20, if different from Report)

18. SUPPLEMENTARY NOTES

APPROVED FOR PUBLIC RELEASE AFR 190-17.

JERRAL F. GUESS, CAPT, USAF
Director of Information

19. KEY WORDS (Continue on reverse side if necessary and identify by block number)

Antenna Arrays
Monopole
Geometrical Theory of Diffractin

20. ABSTRACT (Continue on reverse side if necessary and identify by block number)

Using the Geometrical Theory of Diffraction (GTD), the fields due to a monopole array mounted on an aircraft near the top or bottom were determined and analyzed. The aircraft was modeld as an infinitely long elliptical cylinder. The frequency band of interest was 250 mHz to 400 mHz with an average wavelength of 1 meter. The cross section of the cylinder was modeled as a 2 meter by 4 meter ellipse. The 3 element array was found to have a beam broadening effect when compared to the same array mounted on a ground plane. The array also exhibited a high mobility of its antenna

pattern nulls but with a relativly poor ability to form a single main lobe. The report contains a 26-item bibliography.

VITA

Bruce A. Thieman was born on 9 April 1954 in Dayton, Ohio. He graduted from high school in Mountain Home, Idaho in 1972 and attended the University of Idaho from which he received the degree of Bachelor of Science in Electrical in May 1976. Upon graduation, he received a commission in the USAF through the ROTC program. He was called to active duty in August 1976 and entered the School of Engineering, Air Force Institute of Technology.

Permanent address: 970 Holiday Drive

Mountain Home, Idaho   83647